Petroleum Science 23 (2026) 1650–1674

Contents lists available at ScienceDirect

Petroleum Science

journal homepage: www.keaipublishing.com/en/journals/petroleum-science

Original Paper

Diagenesis and implication for the reservoir quality of the tight sandstone reservoir in the depression zone of foreland basin, Upper Triassic Xujiahe Formation, Western Sichuan Foreland Basin, China: Evidence from petrography and geochemistry

Peng Huang [a,b], Ming-Jie Liu [a,*], Bo Cao [c], Zi-Long Wang [a]

[a] School of Geoscience and Technology, Southwest Petroleum University, Chengdu, 610500, Sichuan, China
[b] Development Division of PetroChina Southwest Oil & Gasfield Company, Chengdu, 610066, Sichuan, China
[c] Sinopec Southwest Oil & Gas Company, Chengdu, 610095, Sichuan, China

ARTICLE INFO

Article history:
Received 16 February 2025
Received in revised form
14 September 2025
Accepted 9 December 2025
Available online 13 December 2025

Edited by Xi Zhang and Jie Hao

Keywords:
Tight sandstone reservoirs
Diagenesis
Reservoir quality
Xujiahe Formation
Foreland basin

ABSTRACT

Tight sandstones are products of complex and various diagenetic events that significantly affect reservoir quality and heterogeneity. In this study, tight sandstones of the Upper Triassic Xu3 Member in the Western Sichuan Foreland Basin were examined as a case study. Petrographic and geochemical analyses were combined to investigate diagenetic variability and its effects on reservoir quality. The sandstone in this zone consisted of coarse-grained to siltstone-grained poorly to moderately sorted sublitharenite and litharenite. And the sandstone exhibits poor physical properties. The diagenesis during the eodiagenetic stage included compaction, dissolution, early-stage quartz cementation, early-stage carbonate cementation (calcite and dolomite), and kaolinite formation. The mesodiagenetic stage encompassed compaction, dissolution, late-stage quartz cementation, intermediate- and late-stage carbonate cementation (ferro-calcite, ankerite, and calcite in fractures), and clay cementation (kaolinite, illite, and chlorite). Compaction destroyed the tight sandstone reservoir to a greater degree than cementation. Specifically, compaction and cementation reduced the initial porosity by 80.70% and 15.50%, respectively. Dissolution emerges as primary constructive diagenesis, promoting the formation of authigenic minerals. The vertical variability in dissolution and cementation within the cycle contributed to increased reservoir heterogeneity. Relatively high-quality reservoirs in the sandstone overlaying sandstone style occurred at the base of the cycle. In the mudstone overlaying sandstone style, relatively high-quality reservoirs developed at both the base and the top of the sandstone layers. These findings enhance our understanding of diagenetic influences on reservoir properties and the distribution of high-quality reservoirs. Consequently, they offer valuable insights for advancing unconventional oil and gas exploration in depression zones of foreland basins.

1. Introduction

With increasing global demand for oil and gas resources, tight sandstone reservoirs, known for their significant exploration potential, have garnered attention (Desbois et al., 2011; Law and Curtis, 2002; Pang et al., 2023). These reservoirs typically exhibit an average permeability of less than 1 mD and an average porosity of less than 10% (Oluwadebi et al., 2018; Zou et al., 2012). Complex and diverse diagenetic alterations commonly occur in tight sandstones, profoundly affecting reservoir quality (Taylor et al., 2010; Xu et al., 2023; Zhang et al., 2015) and affecting hydrocarbon accumulation (Stroker et al., 2013; Xi et al., 2021). Therefore, it is important to elucidate diagenetic types, evolutionary processes, and their impacts on reservoir quality and heterogeneity in tight sandstone reservoirs for the exploration and development of oil

* Corresponding author.
E-mail address: mjliu@swpu.edu.cn (M.-J. Liu).
Peer review under the responsibility of China University of Petroleum (Beijing).

https://doi.org/10.1016/j.petsci.2025.12.016

and gas resources (Fic and Pedersen, 2013; Oluwadebi et al., 2018; Rahman and McCann, 2012).

Tight sandstone reservoirs are prevalent in oil- and gas-producing basins worldwide (Baytok and Pranter, 2013; Kadkhodaie et al., 2021; Liu et al., 2022). Among these basins, foreland basins are significant reservoirs for unconventional oil and gas resources (Boettcher et al., 2010; Kordi, 2019). Notable examples include the Zagros Foreland Basin, the Eastern Venezuela Foreland Basin, the U.S. Rocky Mountain Foreland Basin, as well as the Kuqa Foreland Basin and the West Sichuan Foreland Basin in China (Imin et al., 2020; Liu et al., 2018a). The structural framework of foreland basins is typically comprised of thrust, depression, slope, and uplift zones (Song et al., 2012). Research on tight sandstone hydrocarbons within foreland basins has mainly focused on thrust and slope zones (Xu et al., 2019; Zelilidis and Maravelis, 2015), with a notable gap in the research on the depression zone. Organic-rich mudstones and shales are typically formed within the depression zones of foreland basins (Stroker et al., 2013; Zou et al., 2009). Consequently, the sandstone reservoirs within these depression zones are adjacent to hydrocarbon source rocks. This proximity facilitates short-distance hydrocarbon migration into sandstone reservoirs, and the overlying mudstones act as seals, preventing hydrocarbon escape (Liu et al., 2023a; Worden and Morad, 2000). These characteristics make depression zones highly favorable for hydrocarbon accumulation. Therefore, more attention should be paid to exploring sandstone reservoirs within the depression zones of foreland basins for oil and gas exploration. However, these sandstones within the basin depressions are generally deeper, with intense diagenesis and complex evolutionary processes, resulting in dense and heterogeneous reservoirs that pose challenges in identifying sweet spots (Jiang et al., 2023; Morad et al., 2010). Hence, it is crucial to conduct research on the impacts of diagenesis on reservoir quality and heterogeneity in tight sandstone reservoirs within depression zones to elucidate the mechanisms behind the formation of relatively high-quality reservoirs and their distribution patterns, thereby facilitating the exploration and development of deep tight sandstone reservoirs within these zones.

Previous studies on the reservoir of the Triassic Xujiahe Formation in the study area have predominantly focused on thicker sandstone sections of Xu2 and Xu4 Members (Deng et al., 2022; Gong et al., 2016; Zhong et al., 2020). In contrast, the Xu3 Member has been recognized as a hydrocarbon source rock (Yu et al., 2019). Nonetheless, recent drilling campaigns in the Xu3 Member have yielded abundant tight sandstone gas (Zheng et al., 2020). Despite this, a limited understanding of reservoir quality and heterogeneity has posed substantial challenges for the efficient extraction of tight sandstone gas in the study area. Therefore, this study aimed to address these challenges by investigating diagenesis and its variability, systematically analyzing their effects on reservoir heterogeneity, and identifying the locations of high-quality reservoirs. The specific objectives included (1) exploring the formation mechanisms of different authigenic minerals, (2) reconstructing the diagenetic processes of tight sandstone reservoirs, (3) analyzing the effects of diagenesis on reservoir quality, and (4) discussing its implications for reservoir heterogeneity. These findings offer a valuable reference for the study and development of reservoirs with similar geological characteristics worldwide.

2. Geological setting

The Sichuan Basin, situated in southwestern China, is a petroleum-rich basin in the northwestern region of the Yangtze Block. It overlays both marine and terrestrial foreland basins, spanning approximately 260,000 km^2 in area (Fig. 1(a)) (Lu et al., 2023a; Tan et al., 2023; Zhang, 2022). Over time, the Sichuan Basin has experienced various tectonic movements. The depositional environment underwent significant alteration owing to the opening and closing phases of the Paleo-Tethys Ocean (Jiang et al., 2023; Ma et al., 2023). This can be categorized into distinct periods: from the Ediacaran to the Middle Triassic, the Yangtze Block remained in a stable cratonic environment, with the Sichuan Basin accumulating significant marine sediment (Hao et al., 2008; Liu et al., 2016). Subsequently, during the late Middle Triassic, the collision between the North China and South China Plates induced a transition to a foreland environment, predominantly characterized by riverine-delta-lake systems (Jin et al., 2018; Li et al., 2014; Ma et al., 2007; Mietto et al., 2021). By the Late Cretaceous, the Yanshanian orogeny and the Himalayan orogeny had exposed the Sichuan Basin to erosional processes (Liu et al., 2019; Lu et al., 2023b). Based on its contemporary tectonic features, the Sichuan Basin can be divided into four primary tectonic units, with the West Sichuan Depression situated in the western and northwestern sectors (Fig. 1(a)) (Luo et al., 2019; Qin et al., 2018). The development and evolution of the West Sichuan Depression are primarily controlled by the Longmenshan thrust belt (Jiang et al., 2023; Liu et al., 2012; Sun et al., 2023). During the Late Triassic, the Sichuan Basin transitioned from a passive continental margin to a foreland basin, marking the formation of the Xujiahe Formation (Jiang et al., 2023; Weislogel et al., 2006). With the intensified uplift of Longmenshan, the uplift amplitude increased, causing a shift in the depositional environment of the West Sichuan Depression from marine to continental facies via marine-continental transitional facies (Deng et al., 2022; Jiang et al., 2023; Mietto et al., 2021; Zheng et al., 2019). The stratigraphy of the Xujiahe Formation exhibits a discontinuous relationship with both the basement Leikoupo Formation and the top Baitianba Formation (Fig. 2) (Yu et al., 2022). The Xujiahe Formation is thicker in the depression zone of the Western Sichuan Foreland Basin, with strata gradually thinning from west to east (Fig. 1(c)) (Li et al., 2013; Wu et al., 2021). Throughout the depositional period of the Xujiahe Formation, the region was characterized by lacustrine and delta environments (Fig. 2) (Jin et al., 2018; Lu et al., 2023b). This study focused on the Xu3 sandstone, which developed within the depression zone and was identified as part of a delta–front depositional environment. Based on the regional tectonic features, the study area can be subdivided into six units (Fig. 1(b)) (Wu et al., 2021).

The Xujiahe Formation primarily comprises sandstone, mudstone, and thin coal seam (Jiang et al., 2023; Lai et al., 2018). Within this formation, multiple layers of sandstone and organic-rich mud shale are interactively developed, rendering it a typical tight sandstone gas-producing formation in the Sichuan Basin (Luo et al., 2019; Wang et al., 2023; Yin et al., 2013). Stratigraphically, the Xujiahe Formation is categorized into five members (Xu1–Xu5) from bottom to top (Wang et al., 2015; Yang et al., 2021). The primary stratigraphy of the Xu3 Member is mainly shale with locally developed sandstone and coal seam. Similarly, the Xu1 and Xu5 members are characterized by shale and mudstone, with occasional sandstone development. Conversely, the other members of the Xujiahe Formation are primarily composed of sandstone with locally occurring mudstone and shale (Figs. 1(c) and 2) (Lai et al., 2018; Li et al., 2019b; Wang et al., 2020). In the Xu3 Member of the study area, the hydrocarbon source rocks for the locally developed tight sandstone gas reservoirs primarily comprise extensive mud-shale layers (Li et al., 2019c; Qin et al., 2018). These source rocks predominantly exhibit kerogen types II and III, with total organic carbon contents ranging from 0.5% to 9.7%, averaging 1.96%, and vitrinite reflectance ranging from 0.8% to 1.8% (Guo,

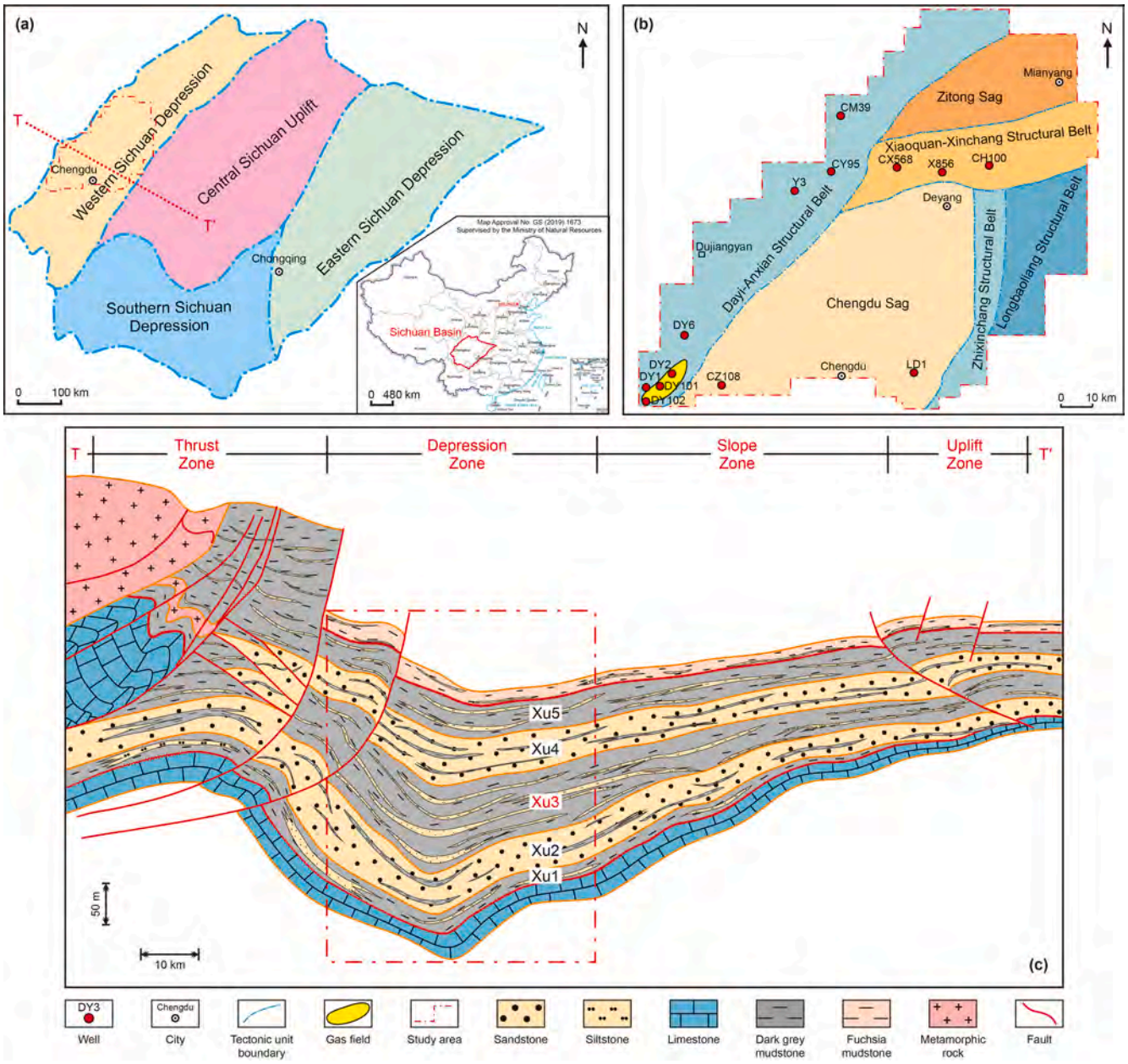

Fig. 1. (**a**) Characteristics of the Sichuan Basin and distribution of tectonic units (modified from Lai et al. (2018) and Wu et al. (2021)). China map from the Standard Map Service System of China (Map Approval No. GS(2019)1673, http://bzdt.ch.mnr.gov.cn). (**b**) Location map of structural units and wells in the depression area. (**c**) Cross-section (T-T' in Fig. 1(a)) illustrating the characteristics of the Upper Triassic strata in the study area (modified from Deng et al. (2022) and Yu et al. (2022)).

2013; Zou et al., 2009). This study focused on tight sandstone gas reservoirs characterized by both proximal and within-source generation (Qin et al., 2018). Analysis of the burial and geothermal history of the Xu3 Member in the study area (Yu et al., 2019; Yang et al., 2021) indicated that the stratigraphy reached its maximum burial depth (exceeding 5 km) during the Late Cretaceous, with a corresponding stratigraphic temperature of 190 °C. Subsequently, the Xu3 stratigraphy underwent gradual uplift accompanied by a decrease in stratigraphic temperature.

3. Samples and methodology

This study focused on the examination and analysis of 202 sandstone core samples sourced from 13 coring wells in the study area (Table S1). These cores, which are whole cores, were provided by Sinopec Southwest Oil & Gas Company. These samples were extracted from the Xu3 Member at depths ranging from 3420 m to 5130 m. The selection criteria for these samples were as follows. First, samples were chosen to ensure comprehensive coverage of the microfacies within the sedimentary subfacies of the Xu3 Member in the study area. Second, representative sedimentary cycles were selected for sampling based on core observations with a sampling interval of less than 1 m. Third, the selection process considered the diverse lithologies present in the sandstone cores observed during the sample collection (Fig. 3).

From the 202 core samples, 202 thin sections were prepared and stained using a mixture of Alizarin Red S and K-ferricyanide. Petrological and mineralogical analyses were performed using a DM2700P Light Microscope. Observations of structural, sorting, and mineral component parameters, along with quantification of the component content using the Gazzi-Dickinson method, were performed under a microscope. Fourteen thin-section samples

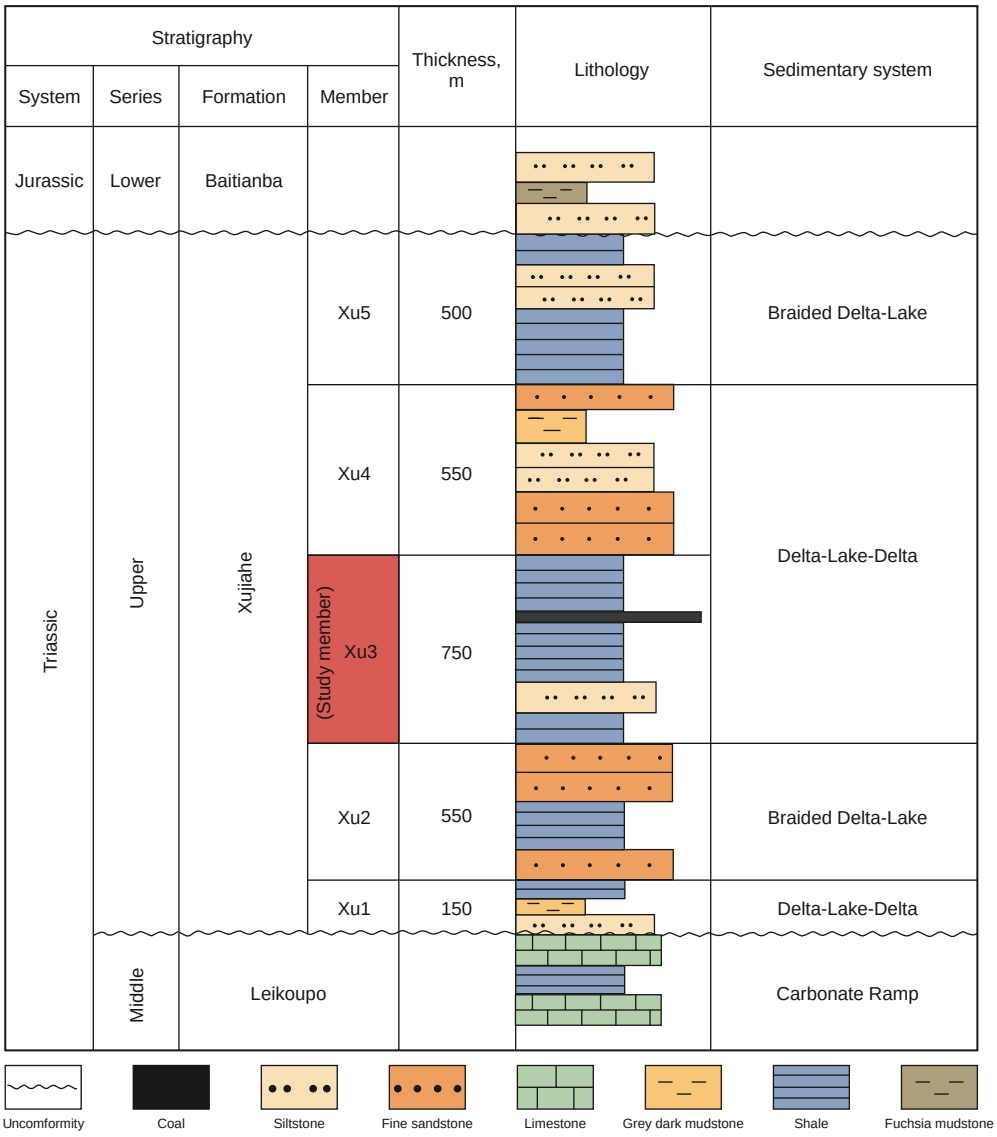

Fig. 2. Stratigraphic sequence of the Xujiahe Formation in the Western Sichuan Depression.

(Table S2) representing various wells and cycle types were selected for cathodoluminescence experiments. A CL8200 MK5 cathodoluminescence microscope was operated at 10–13 kV voltage, 1.0–1.8 mA optical current, and 4.0–5.5 s exposure time. Subsequently, the samples (Table S2) were analyzed using an SU1510 scanning electron microscope. All microscopic analyses were conducted at the Key Laboratory of Natural Gas Geology, Southwest Petroleum University, Sichuan Province, China.

In this study, 81 core samples were analyzed for their physical properties using an HKS-II porosity-permeability instrument. The experiments were conducted at the Experimental Test Center of the School of Geoscience and Technology, Southwest Petroleum University.

In this study, specialized thin sections were prepared to estimate the homogenization temperatures of aqueous inclusions. The experimental analyses were performed using a THMSG600 instrument. For temperature calibration of the geological heating-freezing stage, standard samples of synthetic fluid inclusions were used to adjust the initial parameters of the instrument. The temperature accuracy was ±0.2 °C below room temperature. Within a temperature range of 30–300 °C, the test accuracy of the instrument was ±1 °C. A total of 126 sets of fluid inclusion temperature data were collected. The experiments were conducted at the Key Laboratory of Natural Gas Geology, Southwest Petroleum University, Sichuan Province, China.

Twelve samples from various wells within the study area, selected based on their well-developed and multiple types of carbonate cements, were subjected to carbonate cement carbon and oxygen isotope analyses. Initial sample preparation involved slicing, grinding, and drying. Subsequently, the LMA-10 laser microscope system facilitated micro-area ablation of carbonate cement. The decomposed gases were then analyzed using a MAT251/252 type isotope mass spectrometer with nitrogen as the carrier gas, maintaining an instrumental error of ±0.22‰. The experiment yielded 42 sets of carbonate cement microzone carbon and oxygen isotopic data. All procedures were conducted at the PetroChina Hangzhou Petroleum Geological Research Institute.

Five samples from various wells within the depression zone were selected based on the presence of various types of carbonate

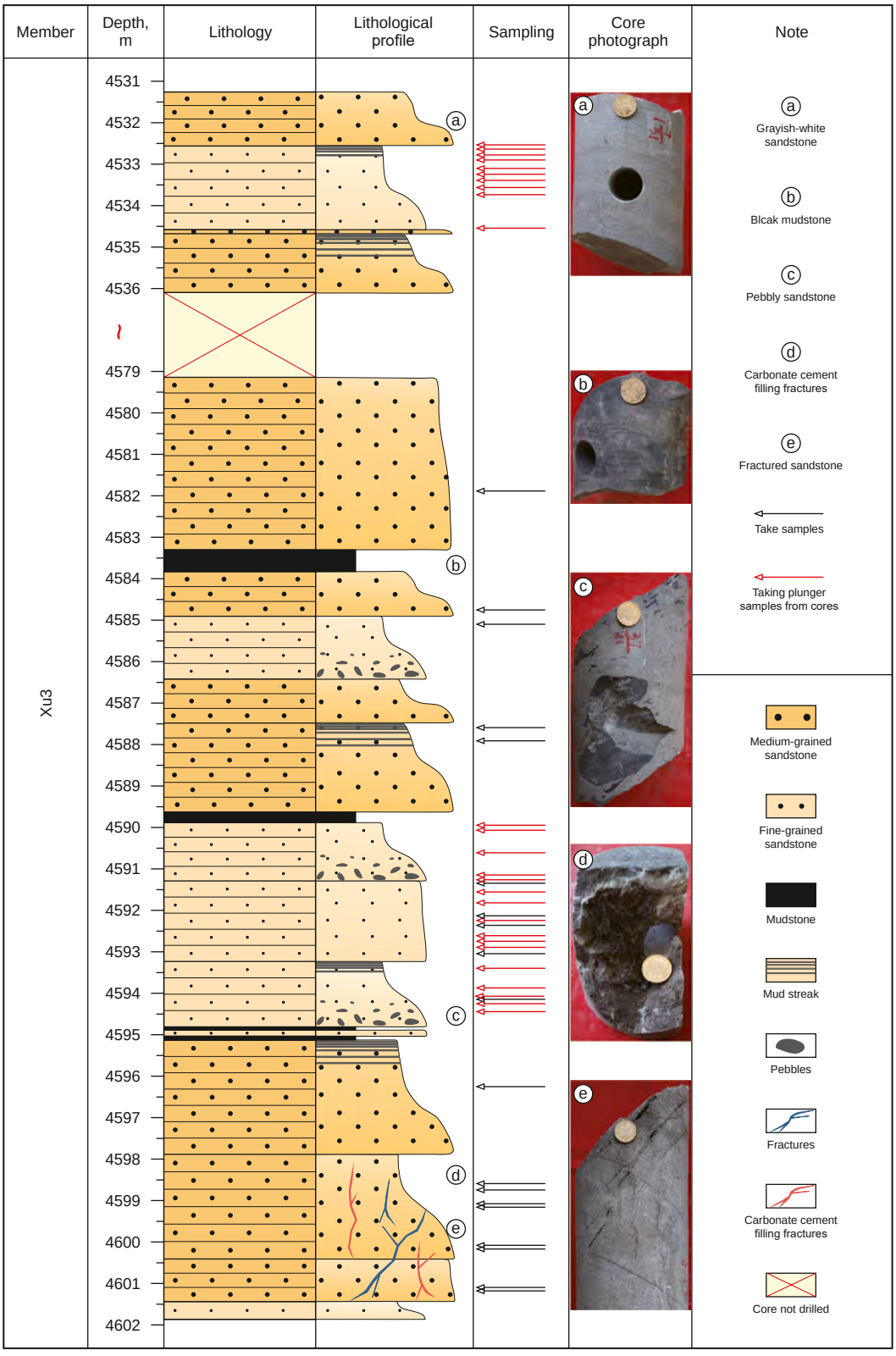

Fig. 3. Core observations and sampling features, a case study of Well DY102.

cements and their suitability for testing and analyzing rare earth elements in these cements. After thin section sample pre-treatment, micro-area ablation of the carbonate cement was conducted using a Newwave 7800 nm UC laser device with a 60 μm laser beam spot. Nitrogen was used as a carrier for the gases produced by cauterized decomposition. The final analysis was conducted using an Agilent 7800 ICP-MS instrument. Eighteen sets of rare earth element (REE) compositional data from carbonate

cement microzones were analyzed. REE data were normalized using the Post-Archean Australian Shale (PAAS) to generate REE + Y compositional pattern diagrams (Nance and Taylor, 1976).

Using point-counted data, the extent of the original porosity degradation due to compaction and cementation was calculated, with the initial porosity assumed to be 40% (Houseknecht, 1987). The detailed calculation process is as follows:

$$\text{Cement} + \text{Intergranular porosity} = \text{Intergranular volume} \quad (1)$$

where cement represents the current volume percentage of cement, intergranular porosity denotes the remaining intergranular pore space, and intergranular volume is the current volume percentage of the intergranular space.

The degree of porosity reduction caused by cementation is calculated by:

$$(\text{Cement} \ / \ 40) \times 100 \quad (2)$$

The impact of compaction on the reduction in the original porosity is determined by:

$$(40 - \text{Intergranular volume}) \ / \ 40 \times 100 \quad (3)$$

Based on these calculations, a plot was constructed to illustrate the relationship between intergranular volume (IGV) and cement volume.

4. Results

4.1. Detrital mineralogy

The Xu3 Member in the study area is primarily composed of grayish-white sandstones and black mudstone (Fig. 3). The lithological composition of the tight sandstone is primarily composed of sublitharenite and litharenite (Fig. 4(a)). Quartz grains constituted 9.6% to 80.3%, averaging 54.3%; feldspar grains ranged from 0.2% to 6.8%, averaging 3.6%; and rock fragments ranged from 5.2% to 73.7%, averaging 24.8%. The sandstone predominantly contained monocrystalline quartz, K-feldspar, microplagioclase feldspar, and plagioclase feldspar. Volcanic fragments (average 4.4%), metamorphic fragments (average 5.8%), and sedimentary fragments (average 14.6%) are the main rock fragment types. Intergranular filler mainly comprises quartz cement (average 4.7%), carbonate cement (average 5.5%), clay minerals (average 3.6%), and matrix (average 2.4%) (Fig. 4(b)). Overall, the grains of the tight sandstone were primarily medium and fine (Fig. 4(c)) with moderate sorting and a predominance of sub-angular to sub-rounded grains.

4.2. Diagenetic events

This study revealed that the Xu3 sandstone in the study area experienced diverse diagenetic effects, including compaction and cementation (carbonate, quartz, and clay minerals) as well as the dissolution of rock fragments and feldspar.

4.2.1. Compaction

The stratigraphic member under study in the area underwent significant burial at depths exceeding 5000 m during the Late Cretaceous (Yu et al., 2019). Consequently, the sandstone reservoirs within this member experienced substantial compaction. Microscopic examination revealed the prevalence of line-contact and line-convex contact between clastic particles (Fig. 5(a)). The deformation of plastic particles (rock fragments) and the fracture of brittle particles (quartz and feldspar) (Fig. 5(a) and (b)) indicated intense mechanical compaction in tight sandstone reservoirs. Furthermore, some particle-to-particle contact margins appeared indistinct under the microscope with evident instances of suture contact (Fig. 5(c)).

A plot illustrating the relationship between intergranular volume (IGV) and cement volume in the tight sandstone reservoir of the stratigraphic member is shown in Fig. 6. Most samples from these reservoirs were found within a 10%–20% intergranular volume range and 5%–20% cement range. The average intergranular volume was 14.7%, and the average intergranular cement volume was 13.8%. Assuming an initial porosity of 40%, the analysis revealed that compaction destroyed 63.25% of the initial

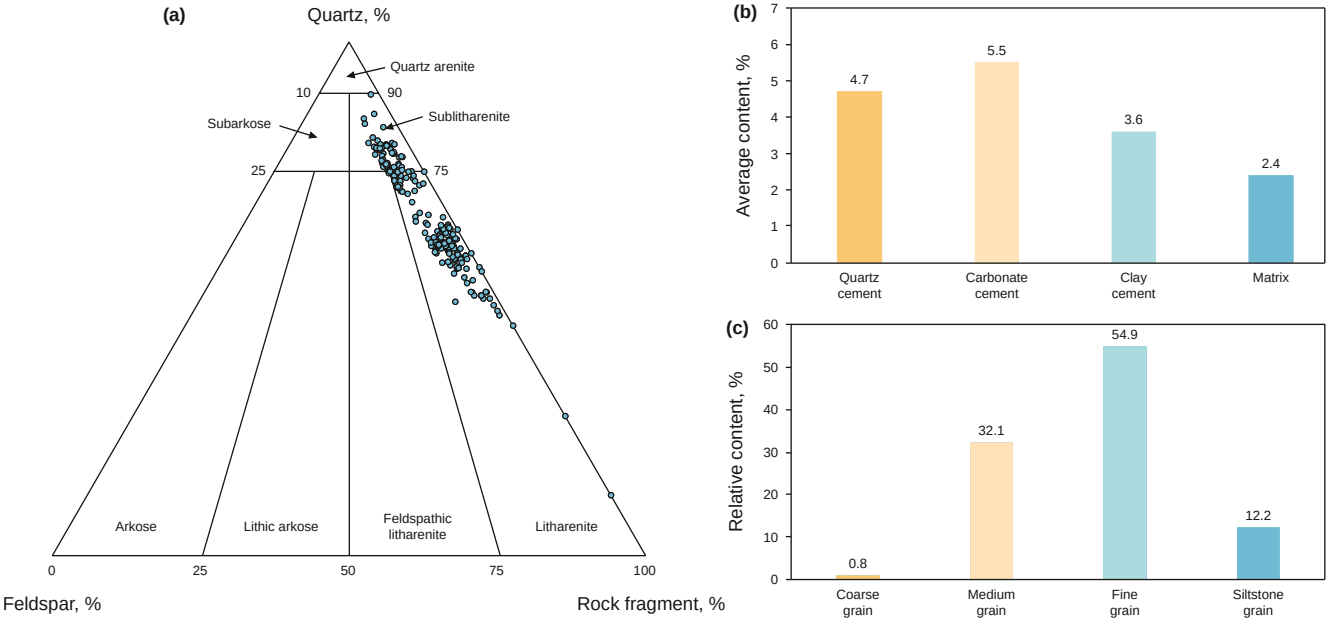

Fig. 4. **(a)** Classification of the Xu3 sandstone according to Folk's scheme (Folk, 1980). **(b)** Cement type and content characterization in the Xu3 sandstone. **(c)** Particle size characterization in the Xu3 sandstone.

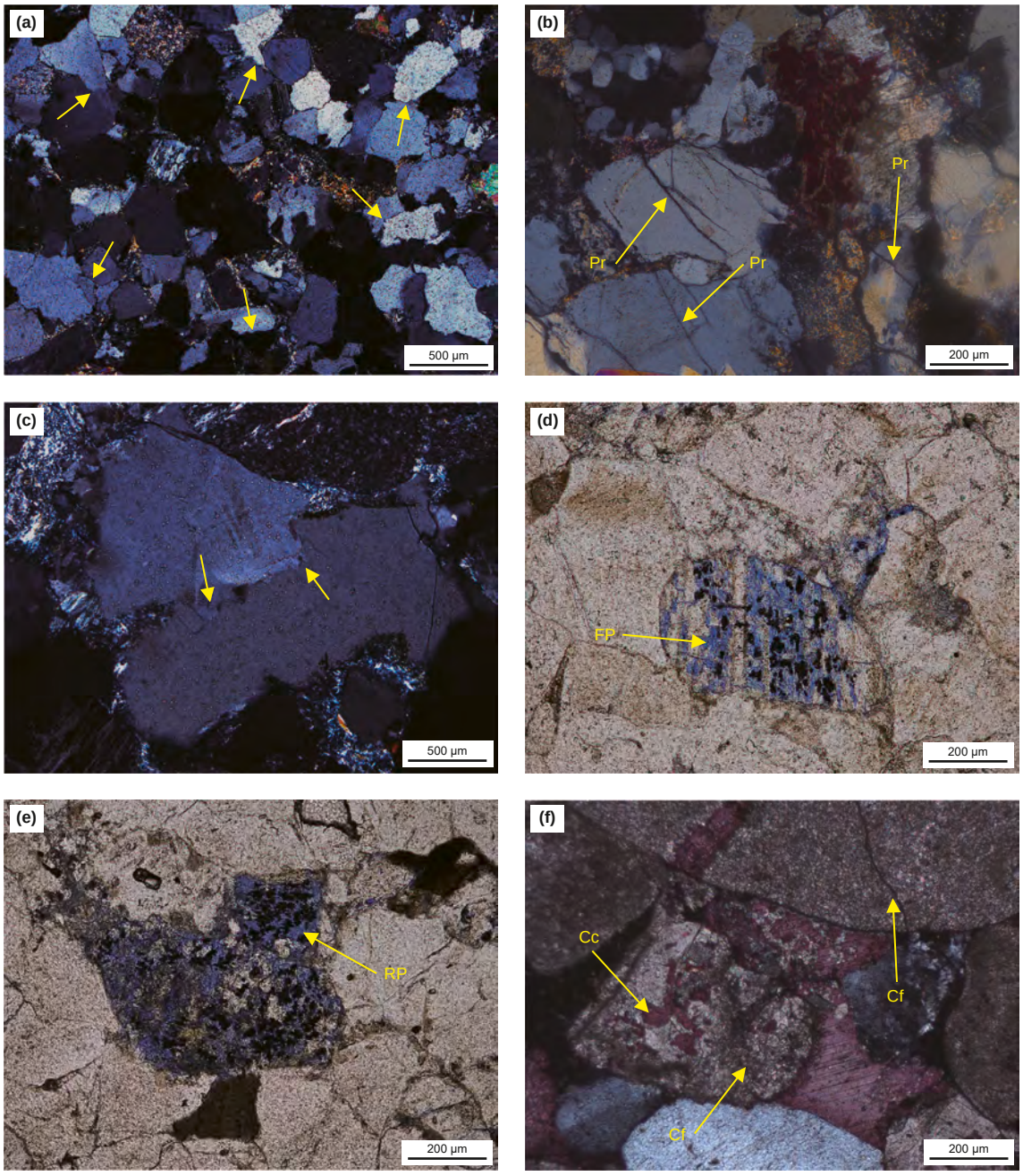

Fig. 5. Images of petrographic features of compaction and dissolution in the Xu3 sandstone. **(a)** Well DY102, 4600.22 m. The particles show concave-convex contact with each other (crossed polarizers). **(b)** Well DY101, 4618.79 m, where the particles rupture (Pr) (crossed polarizers). **(c)** Well DY1, 4637.19 m, where the edges of the particles are not clear from particle to particle (crossed polarizers). **(d)** Well DY102, 4600.22 m, the feldspar grain dissolution forming pore space (FP) (polarized polarizers). **(e)** Well LD1, 3890.22 m, the rock fragment grain dissolution forming pore space (RP) (polarized polarizers). **(f)** Well Y3, 3424.01 m, the carbonate fragment (CF) dissolution forming pore space, with the carbonate cement (Cc) filling the pores (crossed polarizers).

porosity, whereas cementation accounted for 34.50% of the initial porosity loss.

4.2.2. Dissolution

The presence of feldspar and fragmented grains that had undergone dissolution was observed under light microscopy (Fig. 5(d) and (e)). Feldspar grains were primarily dissolved along the cleavage gap (Fig. 5(d)), whereas the dissolution of rock fragments mainly involved aluminum silicate minerals within them (Fig. 5(e)). The intense dissolution of rock fragments can result in complete dissolution, forming mold cavities (Fig. 5(e)). Moreover, carbonate fragments, as one of the rock fragments types, abundant in the research stratigraphic member of the study area, commonly underwent dissolution (Fig. 5(f)). The resulting secondary pores were typically filled with carbonate cement (Fig. 5(f)).

4.2.3. Carbonate cements

In the Xu3 sandstone, various types of carbonate cement were identified, including calcite, dolomite, ferro-calcite, and ankerite (Fig. 7). Calcite and dolomite primarily occupy intergranular and intragranular pores, respectively. Calcite cement was observed to fill intergranular pores through continuous crystalline base-type

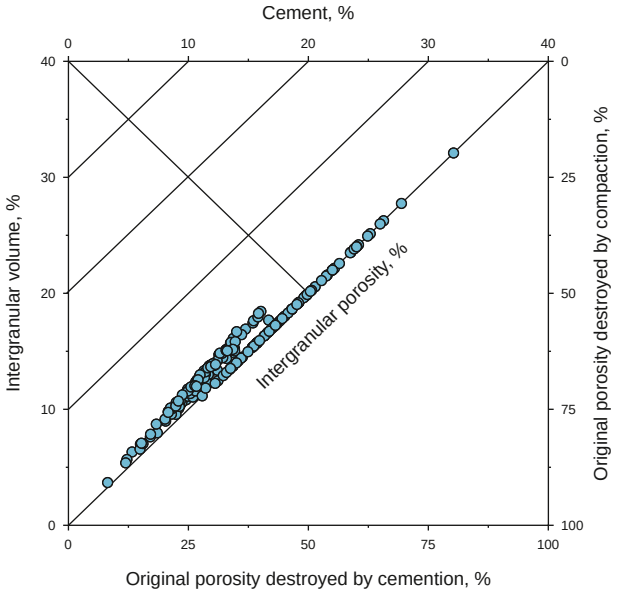

Fig. 6. Plot of intergranular volume (IGV) and cement volume for Xu3 sandstone in the study area.

cementation, creating a nearly "floating" effect on debris particles (Fig. 7(a)) while filling the intragranular dissolution pores (Fig. 7(b)), appearing dark red under cathodoluminescence (Fig. 8(a) and (b)). Additionally, microscopic observations revealed calcite cement filling fractures as coarse, giant crystals, displaying highly automorphic features with two sets of cleavage (Fig. 7(c)) and exhibiting a bright red color under cathodoluminescence (Fig. 8(c) and (d)). Microscopic observation and statistical analysis revealed that calcite cement accounted for 0–18.3% of the mineral component, with an average value of 2.4% (Fig. 9). Dolomite cement, characterized by its typical rhombic crystal shape observed under both light microscopy and scanning electron microscopy (SEM) (Fig. 7(d)–(f)), primarily occupied intergranular pores (Fig. 7(d)) and intragranular dissolution pores (Fig. 7(e)), with contents ranging from 0% to 9.8% and averaging 1.2% (Fig. 9).

Ferro-calcite, which appears dark red under polarized light microscopy (Fig. 7(b), (g), and (h)), filled intergranular residual pores (Fig. 7(d) and (g)–(i)) and intragranular dissolution pores (Fig. 7(b) and (i)). In addition, ferro-calcite was observed to occur in association with the quartz cement (Fig. 7(h)), dolomite (Fig. 7(d)), and calcite (Fig. 7(g)). In cathodoluminescence, ferric-calcite exhibited non-luminescent characteristics (Fig. 8(b)), with contents ranging from 0% to 14.8% and averaging 1.6% (Fig. 9). Ankerite, appearing dark blue under polarized light microscopy, similarly filled intergranular and intragranular dissolution pores (Fig. 7(i)) and was often observed alongside ferro-calcite (Fig. 7(i)), with contents ranging from 0% to 7.9% and averaging 0.3% (Fig. 9).

4.2.4. Clay mineral cements

Light microscopy and SEM analyses identified several types of authigenic clay minerals (Fig. 10(a)–(d)), including kaolinite, illite, and chlorite. These minerals displayed different crystal structures under microscopic examination and occupied various types of pore spaces. Kaolinite predominantly formed vermicular aggregates and leaflets (Fig. 10(a) and (b)), with kaolinite cement filling intergranular pores and encircling quartz overgrowths (Fig. 10(a)). Illite appeared mainly as filamentous and fibrous structures, occupying intergranular pores (Fig. 10(b) and (c)). Chlorite was primarily present as flakes and covered the grain surfaces (Fig. 10(d)).

4.2.5. Quartz cements

Quartz cement primarily manifested as quartz overgrowths and authigenic quartz crystals (Fig. 10(e)–(h)). Quartz overgrowths developed in two stages, predominantly encircling quartz grains coaxially, with evident dust lines delineating their boundaries (Fig. 10(f)). Smaller authigenic quartz crystals also appeared near quartz grains (Fig. 7(h)). Microscopic examination revealed that the quartz cement was enveloped by the growth of various authigenic minerals including calcite (Fig. 10(g)), dolomite (Fig. 10(h)), ferro-calcite (Fig. 10(g)), and clay minerals (Fig. 10(e)).

4.3. Reservoir properties

Thin-section observations revealed that secondary pores were the predominant pore type in the Xu3 tight sandstone. These secondary pores were mainly formed by the dissolution of feldspar and rock fragment particles (Fig. 5(d) and (e)). Generally, the porosity and permeability of the Xu3 Member tight sandstones were low (Table 1). The porosities of the core samples ranged from 1.6% to 6.7% (predominantly from 2% to 5%), with an average of 3.8% (Fig. 11). The permeability varied between 0.021 mD to 0.642 mD (predominantly 0.02 mD to 0.12 mD), with an average of 0.1 mD (Fig. 11). In addition, it was observed that as the porosity increased, permeability increased. Nevertheless, the correlation between porosity and permeability was weak (R^2=0.2674) (Fig. 11).

4.4. Fluid inclusions

These inclusions exhibited both gas and liquid phases at room temperature (Fig. 12(a)–(c)), with the homogenization temperature (T_h) provided in Table 2. In the intergranular carbonate cement, T_h values of aqueous inclusions varied from 67 to 117 °C. Similarly, in the calcite cement within fractures, T_h values varied from 120 to 155 °C. In quartz overgrowths, T_h values of aqueous inclusions ranged from 64 to 125 °C (Fig. 12(d)).

4.5. Carbon and oxygen stable isotope data

The $\delta^{13}C_{PDB}$ values for intergranular carbonate cement ranged from −7.56‰ to 0‰, with an average of −4.68‰, whereas the $\delta^{18}O_{PDB}$ values ranged from −18.68‰ to −6.57‰, averaging −13.07‰. Intragranular carbonate cement exhibited $\delta^{13}C_{PDB}$ values between −7.64‰ and −0.97‰, with an average of −3.96‰, and $\delta^{18}O_{PDB}$ values ranging from −19.87‰ to −5.64‰, averaging of −12.46‰. The $\delta^{13}C_{PDB}$ values for calcite cement filling fractures range from −1.64‰ to −1.06‰, with an average of −1.37‰, and $\delta^{18}O_{PDB}$ values ranged from −20.36‰ to −17.95‰, averaging −19.07‰ (Table 3). Carbon and oxygen isotope data for carbonate cement displayed distinct distribution patterns across the three regions (Fig. 13). Intergranular and intragranular carbonate cement exhibited overlapping isotopic ranges, mainly distributed within regions I and II (Fig. 13). The $\delta^{13}C_{PDB}$ and $\delta^{18}O_{PDB}$ values of calcite filling fractures were primarily distributed in region III (Fig. 13).

4.6. Rare earth element data

The distribution of ΣREE in carbonate cement of the Xu3 sandstone from 0.79 ppm to 548.03 ppm, averaging at 174.16 ppm. Measurement of ΣREE in intergranular and intragranular carbonate cements (calcite, dolomite, ferro-calcite, and ankerite) yielded values ranging from 67.04 to 548.03 ppm, with an average of

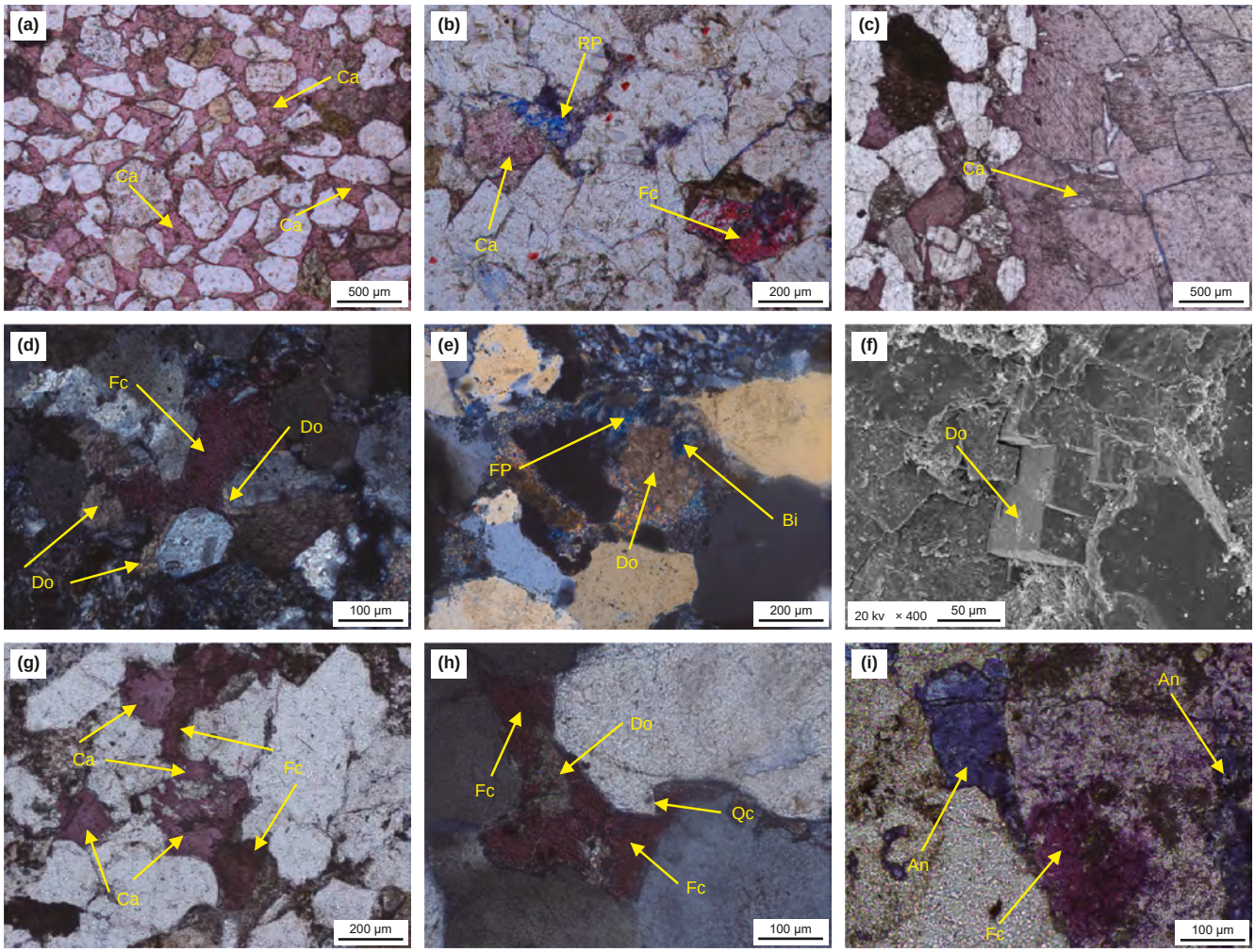

Fig. 7. Images of petrographic features of carbonate cement in the Xu3 sandstone. **(a)** Well LD1, 3890.22 m, calcite cements (Ca) displaying a basal cementation pattern (polarized polarizers). **(b)** Well LD1, 3885.16 m, Ca and ferro-calcite cements (Fc) filling the RP (polarized polarizers). **(c)** Well DY2, 4605.02 m, coarse-microcrystalline Ca filling fractures (polarized polarizers). **(d)** Well CM39, 5119.41 m, characterization of dolomite cements (Do) and Fc, with Fc replacing Do (crossed polarizers). **(e)** Well DY6, 4562.40 m, Do and bitumen (Bi) filling FP (crossed polarizers). **(f)** Well CM39, 5119.41 m, Do possessing a regular crystal shape (SEM). **(g)** Well DY1, 4641.29 m, Fc replacing Ca (polarized polarizers). **(h)** Well DY2, 4605.02 m, Fc replacing quartz cements (Qc) and Do (polarized polarizers). **(i)** Well DY2, 4604.90 m, characterization of ankerite cements (An) (polarized polarizers).

252.27 ppm. Additionally, the ΣREE distribution in calcite cement within fractures ranges from 0.7 to 66.48 ppm, averaging at 17.96 ppm (Table 4). In this study, the earth elements in carbonate cement were standardized using data from the Post-Archean Australian Shale (PAAS) (Table 4).

5. Discussion

5.1. Origin of authigenic minerals

5.1.1. Carbonate cement

Microscopically, calcite filled intergranular pores with connective crystal cementation, whereas clastic particles appear nearly "floating" (Fig. 7(a)), indicating weak stratigraphic compaction and an eodiagenetic stage of calcite and dolomite cement formation (Chen et al., 2016; Grundtner et al., 2017; Luo et al., 2022). Ferro-calcite and ankerite predominantly occupied relatively restricted interparticle pores (Figs. 7(d), (g), (h) and 10(g)), suggesting formation during periods of strong stratigraphic compaction. Concurrently, ferro-calcite replaced calcite (Fig. 7(g)), and dolomite (Fig. 7(d)) under a microscope, indicating later formation relative to calcite and dolomite. Cathodoluminescence analysis revealed a pore-filling carbonate cement with dark red light and no luminescence (Fig. 8(a) and (b)), indicating that two distinct phases were formed by different diagenetic fluids (Lai et al., 2017; Luo et al., 2022). Coarse-giant crystalline calcite filling fractures exhibited bright red cathodoluminescence (Fig. 8(c) and (d)), representing an additional stage of carbonate cement formation (Lin et al., 2020; Xi et al., 2019). The relatively dense fracture-cut sandstone reservoir (Fig. 7(c)) suggested the later formation of calcite-filling fractures.

Carbonate cements primarily develop in alkaline diagenetic environments, whereas quartz cements predominantly form in acidic diagenetic environments (Blake and Walter, 1999; Giles and de Boer, 1990; Taylor et al., 2000). The peak T_h values of aqueous inclusions in quartz overgrowths (Fig. 12(d)) suggested an acidic diagenetic environment that inhibited carbonate cement formation (Dutton, 2008). The formation temperatures of carbonate cements in intergranular and intragranular pores can be determined accordingly. Calcite and dolomite in intergranular and intragranular pores are early-stage carbonate cement (ESCC) formed during the eodiagenetic stage, with diagenetic fluid temperatures ranging from 60 to 90 °C. Ferro-calcite and ankerite in intergranular and intragranular pores are intermediate-stage

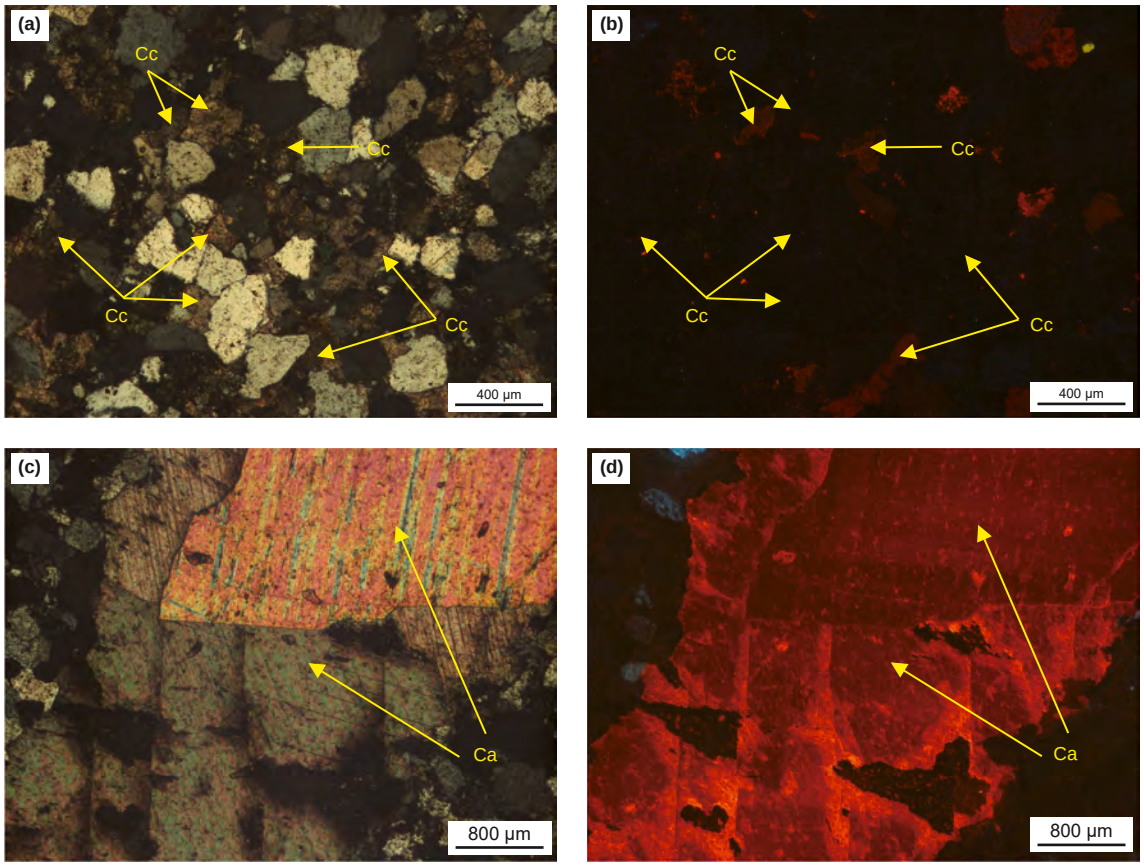

Fig. 8. Images of cathodoluminescence (CL) features of carbonate cement. **(a)** Characterization of carbonate cements (Cc) under a microscope (crossed polarizers), Well CM39 (5119.41 m). **(b)** CL image of (a). **(c)** Characterization of calcite cements (Ca) in fractures under a microscope (crossed polarizers), Well DY102 (4599.16 m). **(d)** CL image of (c).

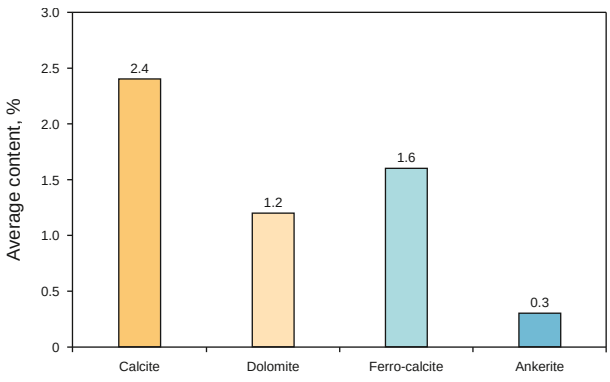

Fig. 9. Histogram of carbonate cement content distribution.

carbonate cement (ISCC) formed during mesodiagenetic stage A, with diagenetic fluid temperatures ranging from 90 to 120 °C. Coarse giant crystalline calcite filling fractures are late-stage carbonate cement (LSCC) formed during mesodiagenetic stage B, with diagenetic fluid temperatures ranging from 120 to 160 °C (Oluwadebi et al., 2018).

Based on the material sources, carbonate cements can be categorized into internal and external formations (Schmid et al., 2006; Wang et al., 2019). Internal mechanisms involve processes such as clastic particle dissolution, contemporaneous carbonate dissolution, silicate mineral hydration, and microbial activity (Sun et al., 2021; Taylor et al., 2000; Yuan et al., 2019; Zhao et al., 2022). External sources primarily include organic matter maturation, hydrothermal fluid activity, and clay mineral transformation (Denny et al., 2017; Longstaffe et al., 2003; Wang et al., 2016).

Oxygen isotopes within carbonate cement serve as indicators of diagenetic fluid composition and mineral precipitation temperature (Bojanowski, 2014; Schmid et al., 2006; Swart, 2015). Hence, region I represented ESCC, region II signified ISCC, and region III indicated LSCC (Fig. 13). Carbon isotopes provide insights into the carbon sources of carbonate cement (Fayek et al., 2001; Taylor et al., 2000). Both ESCC and ISCC exhibited negative carbon isotope characteristics, and their isotopic values correlated strongly with organic matter maturation (Fig. 13) (Taylor et al., 2000; Wang et al., 2019). Both ESCC and ISCC exhibited a flattened shape in the REE + Y pattern, demonstrating a slight enrichment of MREE (Sm~Dy) and a slight deficit in LREE (La~Nd) and HREE (Ho~Lu) (Fig. 14(a) and (b)). The REE + Y pattern of these carbonate cement phases closely resembled that of clay minerals (Fig. 14(d)). This geochemical evidence suggests a close association between the diagenetic fluids of the carbonate cements and mudstone sections (Phan et al., 2019; Shen et al., 2022). In the stratigraphic member of the study area, which featured numerous mudstone layers and locally developed thin coal seams (Fig. 2), mudstone layers were characterized by high organic matter content (Li et al., 2019c; Luo et al., 2019). During the immature stage, mudstones can produce organic acids (Liu et al., 2023b). These acids, along with hydrocarbons produced during the mature stage, enter sandstone reservoirs and dissolve carbonate fragments, generating significant amounts of CO_3^{2-}, Ca^{2+}, Mg^{2+}, and other ions (Yuan et al., 2019; Zheng et al., 2019). Consequently, the carbonate

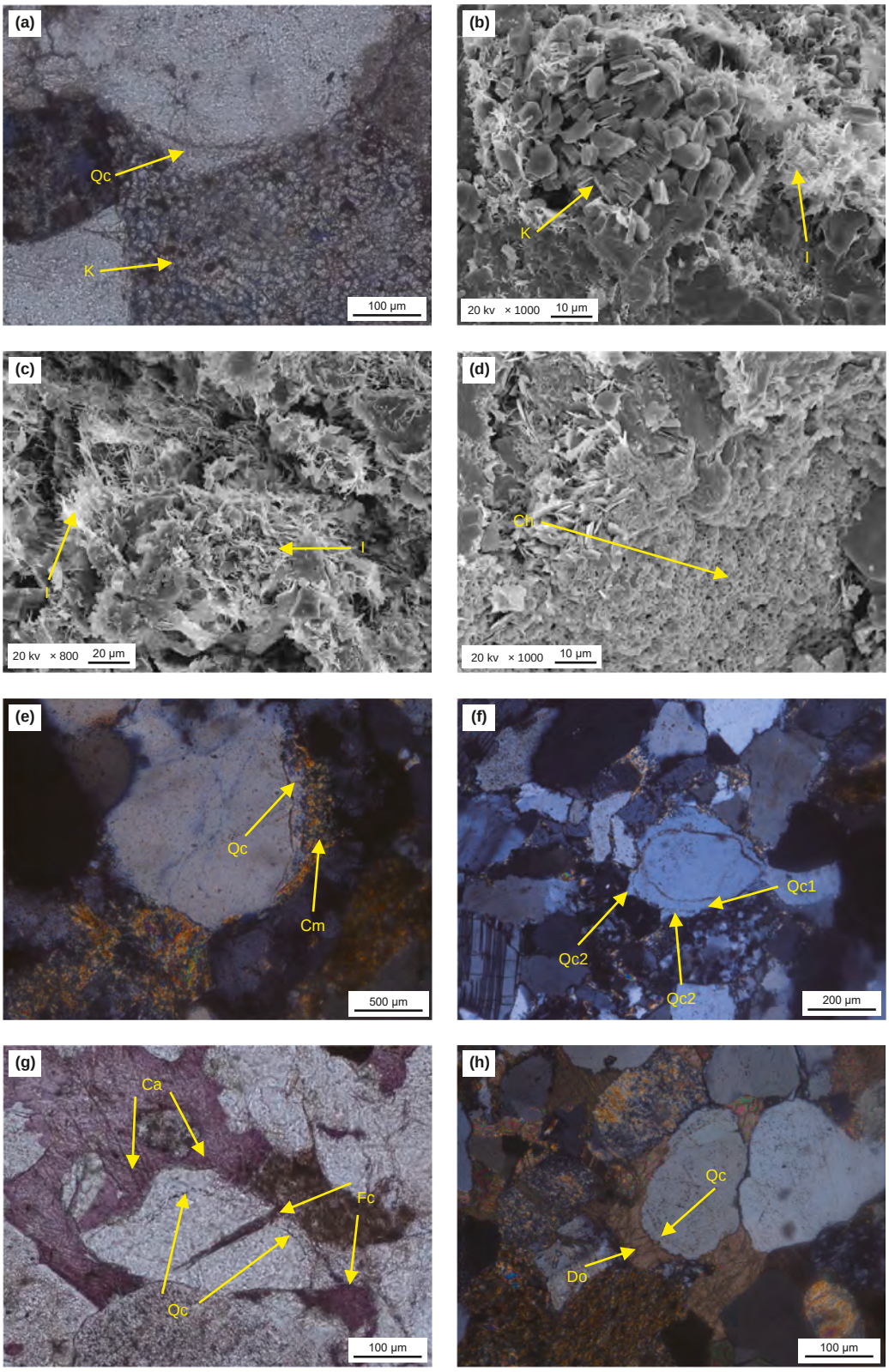

Fig. 10. Images of petrographic features of authigenic minerals in the Xu3 sandstone. **(a)** Well Y3, 3425.24 m, characterization of kaolinite (K) (polarized polarizers). **(b)** Well Y3, 3427.60 m, characterization of K and illite (I) (SEM). **(c)** Well DY6, 4561.72 m, I filling intergranular pores (SEM). **(d)** Well DY2, 4614.76 m, chlorite cements (Ch) on the surface of the particle (SEM). **(e)** Well DY2, 4624.76 m, characterization of clay cements (Cm) replacing quartz overgrowths (Qc) (crossed polarizers). **(f)** Well DY102, 4591.33 m, two stages of quartz overgrowths (Qc1, the first stage; Qc2, the second stage) (crossed polarizers). **(g)** Well CY95, 3523.26 m, characterization of Ca replacing Qc (polarized polarizers). **(h)** Well DY101, 4612.99 m, characterization of Do replacing Qc (crossed polarizers).

Table 1
Reservoir properties of Xu3 tight sandstone in the study area.

Well	Depth, m	Porosity, %	Permeability, mD	Well	Depth, m	Porosity, %	Permeability, mD	Well	Depth, m	Porosity, %	Permeability, mD	Well	Depth, m	Porosity, %	Permeability, mD
DY2	4598.90	3.6079	0.0533	DY2	4617.81	4.8926	0.1292	DY6	4562.97	4.4833	0.2578	DY102	4592.79	3.6764	0.0699
DY2	4600.25	4.8536	0.1298	DY2	4618.08	3.3143	0.0622	DY102	4532.59	3.2740	0.0447	DY102	4592.91	3.7827	0.0643
DY2	4601.52	3.4116	0.1067	DY2	4618.37	3.8298	0.0804	DY102	4532.64	2.4582	0.0350	DY102	4593.42	3.6612	0.0629
DY2	4602.08	3.3654	0.0895	DY2	4618.63	3.9317	0.1038	DY102	4532.81	2.5301	0.0442	DY102	4593.90	2.6244	0.0398
DY2	4602.70	3.3661	0.1041	DY2	4618.93	4.6013	0.0399	DY102	4532.90	2.4071	0.0403	DY102	4594.11	3.0019	0.0582
DY2	4602.76	3.6680	0.4386	DY2	4619.33	3.3454	0.0723	DY102	4533.24	2.3355	0.0472	DY102	4594.24	3.0743	0.0510
DY2	4603.09	3.9178	0.0991	DY2	4619.78	4.4794	0.0826	DY102	4553.30	2.0909	0.0383	DY102	4594.46	2.9743	0.0459
DY2	4604.07	3.5643	0.1518	DY2	4620.06	3.8090	0.0649	DY102	4533.47	2.3406	0.0281	CH100	4334.93	1.5807	0.0304
DY2	4604.90	3.6820	0.0918	DY2	4620.22	3.8046	0.0897	DY102	4533.59	2.4790	0.0430	CM39	5116.73	1.6243	0.0742
DY2	4605.02	5.2157	0.0313	DY2	4620.83	3.8380	0.0825	DY102	4533.72	2.9793	0.0448	X856	3993.81	4.0298	0.0229
DY2	4610.39	4.4097	0.0735	DY2	4621.12	3.7881	0.1319	DY102	4534.56	4.1890	0.0569	X856	3994.82	3.6005	0.0240
DY2	4610.84	4.7480	0.1488	DY2	4621.34	3.5230	0.1172	DY102	4589.92	3.2080	0.0643	X856	3995.55	3.5629	0.0216
DY2	4611.68	3.8887	0.0804	DY6	4560.37	5.5869	0.0513	DY102	4590.04	2.9103	0.0434	X856	3996.04	3.1224	0.0254
DY2	4611.82	4.5026	0.0842	DY6	4560.85	5.9649	0.1051	DY102	4590.68	2.4790	0.0464	X856	3997.53	3.3907	0.0261
DY2	4613.73	4.3772	0.0600	DY6	4561.11	5.3819	0.0955	DY102	4591.26	3.1114	0.0762	X856	3998.19	2.8560	0.0266
DY2	4614.66	4.3748	0.1442	DY6	4561.45	5.3756	0.1747	DY102	4591.33	3.2608	0.0556	X856	3999.03	3.4510	0.0383
DY2	4614.96	5.5389	0.2227	DY6	4561.72	5.8736	0.1906	DY102	4591.55	3.0099	0.0492	X856	3999.73	4.7369	0.0354
DY2	4615.14	6.0179	0.3518	DY6	4562.12	5.9325	0.6423	DY102	4591.85	3.0302	0.0707	X856	4000.41	5.8679	0.0657
DY2	4616.06	2.8461	0.0770	DY6	4562.44	4.3421	0.0486	DY102	4592.26	3.1075	0.0615	X856	4000.66	6.6778	0.0820
DY2	4616.30	4.4379	0.1041	DY6	4562.79	4.6638	0.2976	DY102	4592.68	3.1407	0.0591	X856	4001.77	6.2086	0.0741
DY2	4617.43	4.6982	0.1658												

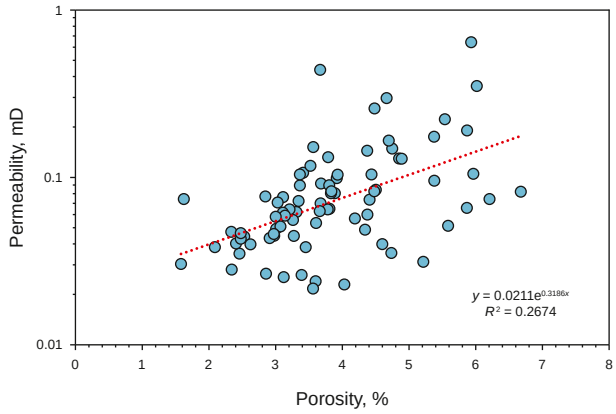

Fig. 11. Characteristics of Xu3 sandstone reservoir properties.

fragment content exhibited a positive correlation with the carbonate cement content (Fig. 15(a)). Additionally, organic acid decarboxylation can further produce CO_3^{2-} (Ma et al., 2017; Wang et al., 2019), providing material sources for the formation of carbonate cements. During the mesodiagenetic stage, stronger compaction led to the influx of numerous metal ions from mudstone layer segments into sandstone reservoirs alongside organic acids, including Ca^{2+}, Fe^{2+}, Mg^{2+}, and other ions (Bjørlykke and Jahren, 2012; Lin et al., 2020). At this stage, the availability of Fe^{2+} ions facilitated the formation of Fe-bearing carbonate cement (ferro-calcite and ankerite) (Liu and Xiong, 2021; Liu et al., 2022). Consequently, the formation of ESCC and ISCC are associated with organic matter maturation and the dissolution reprecipitation of carbonate rock fragments.

The $\delta^{13}C_{PDB}$ and $\delta^{18}O_{PDB}$ values of the LSCC exhibited a strong dissimilarity with those of the previous two-stage carbonate cement (Fig. 13). The rare earth element (REE) pattern of the LSCC revealed enrichment in MREE (Sm~Dy) and a significant positive anomaly of Eu, while LREE (La~Nd) and HREE (Ho~Lu) showed relative deficits (Fig. 14(c)). The distribution characteristics and rare earth content of LSCC closely resembled those of hydrothermal fluids and marine carbonates (Fig. 14(d)) (Debruyne et al., 2016; Phan et al., 2019; Xiong et al., 2016). Given the presence of marine carbonatite stratigraphy beneath the Xujiahe Formation and the development of faults connecting the deep marine stratigraphy within the Xu3 Member (Luo et al., 2013; Li et al., 2019a), hydrothermal fluids from deeper formations dissolved marine carbonate formations. These fluids ascended along fractures, and as the temperature and pressure decreased, late-stage calcite crystals precipitated directly from the fluids to fill the fractures (Lee et al., 2003; Xiao et al., 2020). As a result, this stage of carbonate cement is attributed to hydrothermal activity as the primary mechanism for its formation.

5.1.2. Quartz cements and clay minerals

The sources of SiO_2 that contribute to quartz cement formation can be categorized into internal and external sources (Gier et al., 2008; Liu and Xiong, 2021). Internal sources primarily involve biogenic origins, the pressure dissolution of quartz grains, clay mineral transformation, and feldspar grain dissolution (Hyodo et al., 2014; Yu et al., 2022). Microscopic examination revealed two distinct periods of quartz overgrowth in the tight sandstone reservoirs of the study area (Fig. 10(f)), indicating two-stage quartz cementation. Based on the analysis of the T_h values of aqueous inclusions within quartz overgrowths, the temperature of the

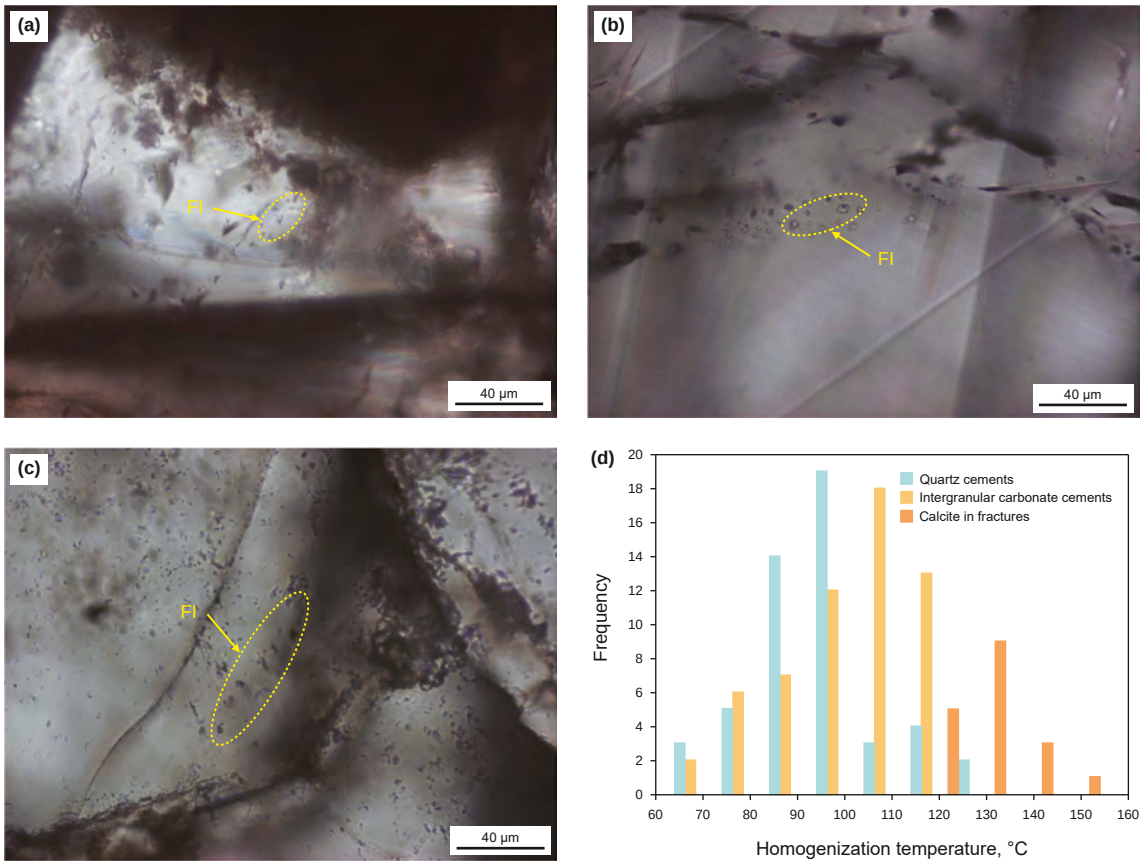

Fig. 12. Characteristics of aqueous inclusions in the Xu3 sandstone of the study area. **(a)** Images of petrographic features of fluid inclusions (FI) in carbonate cements at room temperature. **(b)** Images of petrographic features of FI in carbonate cements in fracture temperature. **(c)** Images of petrographic features of FI in the quartz cement at room temperature. **(d)** Histogram of homogenization temperature (T_h) for fluid inclusions.

diagenetic fluid responsible for quartz cement formation was determined (Oluwadebi et al., 2018; Xi et al., 2019). Early-stage quartz cement crystallization and precipitation occurred at temperatures below 90 °C during the eodiagenetic stage, whereas late-stage quartz cement crystallization and precipitation occurred between 90 and 130 °C during the mesodiagenetic stage (Fig. 12(d)). Through dissolution processes, feldspar and rock fragment particles can release abundant ions such as Al^{3+}, Mg^{2+}, and Si^{4+} (Liu et al., 2016; Leitner et al., 2020), which can precipitate as quartz cement in acidic environments (Gardner et al., 2021). Given the predominance of carbonate rock fragments in the stratigraphic members of the study area, the material supplied by rock fragment dissolution for quartz cement formation was relatively limited. This limitation resulted in a weak positive correlation between quartz cement content and rock fragment content (Fig. 15(b)). The dissolution of K-feldspar particles likely contributed to the formation of SiO_2 (Fig. 15(c)) and may have also promoted the development of clay minerals (Fig. 15(d)) (Bjørlykke and Jahren, 2012; Taylor et al., 2010). The specific chemical reactions are as follows:

$$2KAlSi_3O_8 + 2H^+ + H_2O = Al_2Si_2O_5(OH)_4 + 2K^+ + 4SiO_2 \quad (4)$$

where $KAlSi_3O_8$, $Al_2Si_2O_5(OH)_4$, and SiO_2 are K-feldspar, kaolinite, and quartz, respectively.

During the mesodiagenetic stage, kaolinite formed by feldspar dissolution underwent a transformation into illite (Fig. 10(b)). Hence, the feldspar content was positively associated with the illite content (Fig. 15(d)). The products of this transformation can serve as material sources for quartz cement formation (Ma et al., 2017; Peltonen et al., 2009; Xi et al., 2019). The specific chemical reactions are as follows:

$$2KAlSi_3O_8 + Al_2Si_2O_5(OH)_4 = KAl_3Si_3O_{10}(OH)_2 + 2SiO_2 + 2H_2O \quad (5)$$

where $KAl_3Si_3O_{10}(OH)_2$ is illite.

Moreover, suture contacts between some quartz grains were evident in the tight sandstone, indicating pressure dissolution between quartz grains (Fig. 5(c)). This interaction provided a silica source for quartz cement formation (Rezaee and Tingate, 1997; Worden and Morad, 2000). However, the amount of silica supplied by this pressure dissolution was relatively small, making it a secondary mechanism for quartz cement formation (Chen et al., 2024; Ma et al., 2017; Yu et al., 2022). Consequently, the diagenetic fluids involved in the two stages of quartz cementation in the stratigraphic member of the study area were primarily associated with acidic organic fluids. The diagenetic mechanism involved the dissolution of feldspar particles and the transformation of clay minerals.

5.2. Diagenetic sequence

5.2.1. Eodiagenesis

The eodiagenetic stage typically refers to a period characterized by shallow burial depths and diagenetic temperatures ranging from 30 to 90 °C (Fig. 16) (Chen et al., 2016; Qian et al., 2020).

Table 2
T_h data for aqueous inclusions in carbonate and quartz cements.

Well	Depth, m	Host mineral	T_h, °C	Well	Depth, m	Host mineral	T_h, °C	Well	Depth, m	Host mineral	T_h, °C
DY102	4599.16	C-F	123	DY2	4605.02	Q-C	97	Y3	3424.01	Inter-C	113
DY102	4599.16	C-F	142	DY2	4605.02	Q-C	94	Y3	3424.01	Inter-C	105
DY102	4599.16	C-F	120	DY2	4605.02	Q-C	125	Y3	3424.01	Inter-C	113
DY102	4599.16	C-F	123	DY2	4605.02	Q-C	123	Y3	3424.01	Inter-C	109
DY102	4599.16	C-F	134	DY2	4605.02	Inter-C	102	Y3	3424.01	Inter-C	102
DY102	4599.16	C-F	130	DY2	4605.02	Inter-C	98	Y3	3424.01	Inter-C	108
DY102	4599.16	C-F	132	DY2	4605.02	Inter-C	94	DY2	4611.68	Inter-C	87
DY102	4599.16	C-F	122	DY2	4605.02	Inter-C	103	DY2	4611.68	Inter-C	104
DY102	4599.16	C-F	132	DY2	4605.02	Inter-C	102	DY2	4611.68	Inter-C	94
DY102	4599.16	C-F	121	DY2	4605.02	Inter-C	109	DY2	4611.68	Inter-C	104
DY2	4605.02	C-F	138	DY2	4605.02	Inter-C	114	DY2	4611.68	Inter-C	106
DY2	4605.02	C-F	131	DY2	4605.02	Inter-C	97	DY2	4611.68	Q-C	93
DY2	4605.02	C-F	136	DY2	4605.02	Inter-C	73	DY2	4611.68	Q-C	97
DY2	4605.02	C-F	132	DY2	4605.02	Inter-C	93	DY2	4611.68	Q-C	94
DY2	4605.02	C-F	137	DY2	4605.02	Inter-C	117	DY2	4611.68	Q-C	84
DY2	4605.02	C-F	148	DY2	4605.02	Inter-C	109	DY2	4611.68	Q-C	80
DY2	4605.02	C-F	147	Y3	3424.01	Inter-C	115	X856	3996.04	Inter-C	71
DY2	4605.02	C-F	155	Y3	3424.01	Inter-C	115	X856	3996.04	Inter-C	68
DY2	4605.02	Q-C	92	Y3	3424.01	Inter-C	116	X856	3996.04	Inter-C	82
DY2	4605.02	Q-C	87	Y3	3424.01	Inter-C	112	X856	3996.04	Inter-C	109
DY2	4605.02	Q-C	81	Y3	3424.01	Inter-C	113	X856	3996.04	Inter-C	82
DY2	4605.02	Q-C	84	Y3	3424.01	Inter-C	107	X856	3996.04	Inter-C	79
X856	3996.04	Q-C	87	CY95	3523.26	Q-C	114	CX568	4080.73	Q-C	94
X856	3996.04	Q-C	89	CY95	3523.26	Inter-C	75	CX568	4080.73	Q-C	87
X856	3996.04	Q-C	117	CY95	3523.26	Inter-C	82	CX568	4080.73	Q-C	102
X856	3996.04	Q-C	99	CY95	3523.26	Inter-C	95	CX568	4080.73	Inter-C	79
DY102	4532.81	Inter-C	97	CY95	3523.26	Inter-C	96	CX568	4080.73	Inter-C	86
DY102	4532.81	Inter-C	114	CY95	3523.26	Inter-C	67	CX568	4080.73	Inter-C	97
DY102	4532.81	Inter-C	102	DY102	4601.12	Q-C	95	CX568	4080.73	Inter-C	78
DY102	4532.81	Inter-C	105	DY102	4601.12	Q-C	91	CX568	4080.73	Inter-C	106
DY102	4532.81	Inter-C	94	DY102	4601.12	Q-C	98	CH100	4331.04	Q-C	115
DY102	4532.81	Q-C	98	DY102	4601.12	Q-C	84	CH100	4331.04	Q-C	92
DY102	4532.81	Q-C	97	DY102	4601.12	Q-C	89	CH100	4331.04	Q-C	84
DY102	4532.81	Q-C	102	DY102	4601.12	Q-C	97	CH100	4331.04	Q-C	87
DY102	4532.81	Q-C	87	DY102	4601.12	Q-C	112	CH100	4331.04	Q-C	91
DY102	4532.81	Q-C	92	DY102	4601.12	Inter-C	113	CH100	4331.04	Q-C	72
CY95	3523.26	Q-C	71	DY102	4601.12	Inter-C	106	CH100	4331.04	Q-C	67
CY95	3523.26	Q-C	64	DY102	4601.12	Inter-C	97	CH100	4331.04	Inter-C	111
CY95	3523.26	Q-C	91	CX568	4080.73	Q-C	77	CH100	4331.04	Inter-C	113
CY95	3523.26	Q-C	86	CX568	4080.73	Q-C	79	CH100	4331.04	Inter-C	82
CY95	3523.26	Q-C	96	CX568	4080.73	Q-C	68	CH100	4331.04	Inter-C	95
CY95	3523.26	Q-C	101	CX568	4080.73	Q-C	79	CH100	4331.04	Inter-C	86

*T_h: Homogenization temperature; C-F: Calcite in fractures; Inter-C: Intergranular carbonate cements; Q-C: Quartz cements.

During this stage, in the Xu3 tight sandstone, the sediment layers had a certain burial depth, leading to the compaction of clastic particles by overlying pressure (Gardner et al., 2021; Liu et al., 2019). Organic matter within mudstone layers and coal seams generated organic acids during their immature stage, which infiltrated the sandstone layers (Li et al., 2019c; Taylor et al., 2010). Consequently, the pore fluids during this period consisted primarily of organic acidic fluids, triggering dissolution reactions with feldspars and rock fragments. This dissolution produced ions, such as Ca^{2+}, Mg^{2+}, Al^{3+}, SiO_2, and CO_3^{2-} (Liu et al., 2016; Leitner et al., 2020). Under acidic conditions, these ions crystallized and precipitated to form quartz cement and kaolinite (Fig. 10(a) and (f)–(h)) (Liu et al., 2016; Oluwadebi et al., 2018). As diagenesis progressed, the depletion of H^+ ions in acidic diagenetic fluids led to the influx of numerous alkaline metal cations, causing the transition of diagenetic fluids from acidic to alkaline (Dutton, 2008; Luo et al., 2022). In this alkaline environment, ions such as Ca^{2+}, Mg^{2+}, and CO_3^{2-} in the diagenetic fluid underwent crystallization and precipitation, forming calcite and dolomite (Fig. 7(a), 10(g) and (h)) (Dutton and Loucks, 2010; Xi et al., 2015).

5.2.2. Mesodiagenesis

The mesodiagenetic stage typically denotes a period characterized by a specific stratigraphic burial depth and diagenetic temperatures ranging from 90 to 140 °C (Fig. 16) (Chen et al., 2016). During the transition from the eodiagenetic stage to the mesodiagenetic stage, the stratigraphic burial depth continued to increase, accompanied by an increase in the overburden pressure on the sandstone reservoirs and the intensity of compaction (Liu and Xiong, 2021; Oluwadebi et al., 2018). Simultaneously, eodiagenesis and compaction resulted in a significant loss of intergranular pore space, gradually densifying the reservoir during the middle diagenetic stage (Wang et al., 2019; Zheng et al., 2019). Consequently, the impact of compaction on sandstone reservoirs gradually decreased. During the mesodiagenetic stage, as the organic matter within the mudstone layers reached the hydrocarbon generation threshold, abundant organic acidic fluids were produced. Concurrently, compaction forces facilitated the migration of metal ions such as Fe^{2+}, Ca^{2+}, and Mg^{2+}, from mudstone to sandstone reservoirs alongside organic acidic fluids (Liu et al., 2022). Therefore, the predominant diagenetic fluids within the

Table 3
Carbon–oxygen isotopic compositions of carbonate cement in the Xu3 sandstone.

Well	Depth, m	$\delta^{13}C_{PDB}$, ‰	$\delta^{18}O_{PDB}$, ‰	Cement type
DY102	4590.68	−6.58	−14.47	Inter-C
DY102	4590.68	−5.98	−15.19	Inter-C
DY102	4590.68	−7.56	−18.28	Inter-C
DY2	4611.68	−3.47	−9.84	Inter-C
DY2	4611.68	−3.24	−12.69	Inter-C
DY2	4618.93	−3.95	−10.37	Inter-C
CM39	5119.41	−7.21	−17.35	Inter-C
CM39	5119.41	−7.16	−18.68	Inter-C
CY95	3523.26	−6.53	−18.62	Inter-C
CY95	3523.26	−3.02	−8.63	Inter-C
CY95	3523.26	−6.87	−15.14	Inter-C
X856	3996.04	−6.32	−15.59	Inter-C
X856	3996.04	−6.63	−16.58	Inter-C
Y3	3425.24	−4.07	−11.26	Inter-C
Y3	3425.24	−3.30	−12.46	Inter-C
Y3	3425.24	−3.91	−9.42	Inter-C
Y3	3424.01	−2.36	−9.36	Inter-C
Y3	3424.01	−0.80	−6.57	Inter-C
Y3	3424.01	0.00	−7.79	Inter-C
DY102	4532.81	−7.64	−15.97	Intra-C
DY102	4532.81	−6.87	−16.23	Intra-C
DY102	4590.68	−6.89	−17.43	Intra-C
DY102	4590.68	−6.36	−17.91	Intra-C
DY2	4611.68	−2.94	−12.57	Intra-C
DY2	4611.68	−1.39	−5.85	Intra-C
DY2	4618.93	−1.49	−11.35	Intra-C
DY2	4618.93	−1.63	−12.16	Intra-C
DY2	4618.93	−1.69	−11.62	Intra-C
CM39	5119.41	−2.14	−7.11	Intra-C
CM39	5119.41	−3.35	−7.68	Intra-C
CY95	3523.26	−6.95	−19.87	Intra-C
CY95	3523.26	−7.15	−16.23	Intra-C
X856	3996.04	−1.73	−5.64	Intra-C
X856	3996.04	−3.15	−11.26	Intra-C
Y3	3425.24	−7.01	−19.07	Intra-C
Y3	3424.01	−0.97	−7.62	Intra-C
Y3	3424.01	−1.84	−8.67	Intra-C
DY102	4599.16	−1.25	−18.79	C-F
DY102	4599.16	−1.06	−17.95	C-F
DY102	4599.16	−1.48	−18.14	C-F
DY2	4605.02	−1.42	−20.11	C-F
DY2	4605.02	−1.64	−20.36	C-F

*Inter-C: Intergranular Cements; Intra-C: Intragranular Cements; C-F: Calcite in fractures.

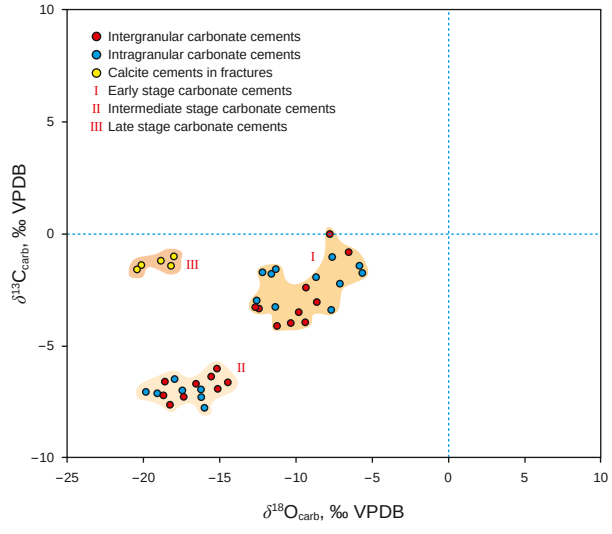

Fig. 13. Scatter plot of $\delta^{13}C_{PDB}$ and $\delta^{18}O_{PDB}$ values for carbonate cements in the Xu3 sandstone of the study area.

Table 4
REE data for carbonate cement. The data used in the experiments are presented in ppm. The normalization formula used was REEN=REE/PAAS.

Well	Depth, m	Sample	Type	La	Ce	Pr	Nd	Sm	Eu	Gd	Tb	Dy	Y	Ho	Er	Tm	Yb	Lu
X856	3996.04	1	CII	65.4	197.1	27.65	109.16	24.09	6.02	27.48	4.29	26.68	158.2	5.35	14.4	1.9	12.23	1.78
X856	3996.04	2	CII	43.9	162.5	25.86	114.6	28.48	6.74	31.67	4.79	28.63	167.2	5.41	13.86	1.751	10.66	1.435
X856	3996.04	3	CII	64.7	204.2	27.83	106.7	23.79	5.71	24.14	3.632	21.61	118.5	4.037	10.48	1.324	8.52	1.208
X856	3996.04	4	CII	64.7	208.3	30.1	120.7	26.68	6.03	28.56	4.35	26.6	158.5	5.2	13.32	1.683	10.36	1.449
X856	3996.04	5	CII	20.53	66.4	8.97	34.9	7.66	1.826	7.87	1.14	6.84	37.8	1.244	3.15	0.408	2.51	0.374
CM39	5119.41	1	CII	37.7	82	10.5	44.1	11.31	3.152	13.83	2.258	13.25	75.3	2.509	6.28	0.771	4.65	0.634
DY2	4618.93	1	CII	15.9	28.8	3.19	12.59	2.89	0.861	3.29	0.498	3.17	24.96	0.64	1.809	0.24	1.51	0.207
DY2	4618.93	2	CII	31.14	65.63	7.554	29.15	6.44	1.617	6.63	1.054	6.673	46.2	1.347	3.693	0.481	2.84	0.37
DY2	4618.93	3	CII	20.21	41.33	4.62	17.24	3.673	1.017	3.77	0.62	3.76	25.64	0.796	2.124	0.27	1.59	0.225
DY2	4618.93	4	CII	25.29	41.2	4.27	16.33	3.11	0.906	3.668	0.503	3.168	28.88	0.648	1.764	0.2143	1.173	0.1651
DY2	4532.81	5	CII	15.24	17.2	2.437	9.74	2.139	0.697	2.97	0.491	3.58	33.3	0.813	2.293	0.278	1.718	0.2299
DY2	4532.81	6	CII	13.56	21.3	2.52	10.45	2.82	0.97	3.95	0.651	4.32	28.5	0.94	2.66	0.366	2.22	0.315
DY102	4599.16	1	CF	3.23	11.09	1.958	12.49	7.57	6.59	11.2	1.298	6.26	37.17	1.004	2.201	0.24	1.216	0.1333
DY102	4599.16	2	CF	0.214	0.267	0.0385	0.233	0.082	1.26	0.152	0.012	0.0503	0.647	0.0071	0.014	0.0016	0.002	0.00044
DY102	4599.16	3	CF	2.135	4.01	0.627	4.15	2.18	2.61	3.68	0.337	1.43	12.13	0.217	0.429	0.0309	0.084	0.0078
DY102	4599.16	4	CF	0.2	0.424	0.071	0.466	0.188	1.17	0.33	0.0277	0.121	1.11	0.0212	0.0444	0.0023	0.0147	0.00127
DY102	4599.16	5	CF	0.0543	0.155	0.063	0.121	0.055	0.1994	0.078	0.0079	0.0308	0.231	0.0116	0.0056	0.001	0.007	0.00047
DY102	4599.16	6	CF	0.756	1.64	0.306	2.26	1.45	2.12	2.64	0.246	1.106	8.64	0.159	0.306	0.0251	0.093	0.0096
		PAAS		38.2	79.6	8.83	33.9	5.55	1.08	4.66	0.774	4.68	27	0.991	2.85	0.405	2.82	0.433

*CII: Carbonate cement filling intragranular and intergranular pores; CF: Carbonate cement filling fractures; ESCC: Early stage carbonate cement; ISCC: Intermediate stage carbonate cement; LSCC: Late stage carbonate cement.

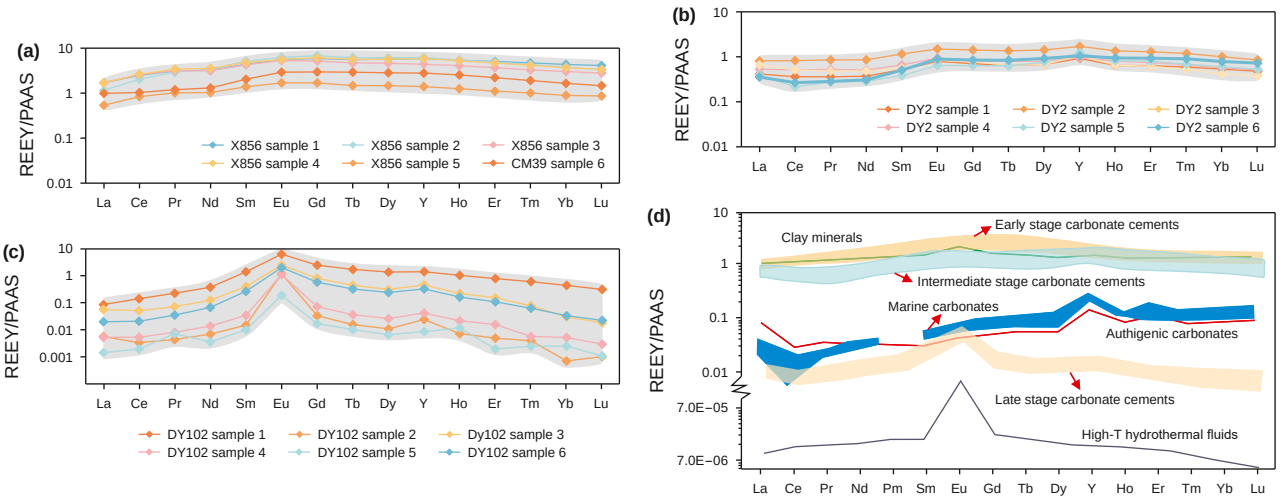

Fig. 14. Post-Archean Australian Shale (PAAS)-normalized REE + Y patterns of carbonate cement in the Xu3 tight sandstone. **(a–c)** REE + Y patterns for early-, intermediate-, and late-stage carbonate cements. **(d)** PAAS-normalized REE + Y patterns of typical fluids and sediments (adapted from Debruyne et al. (2016), Sylvestre et al. (2017), and Zhao et al. (2019)).

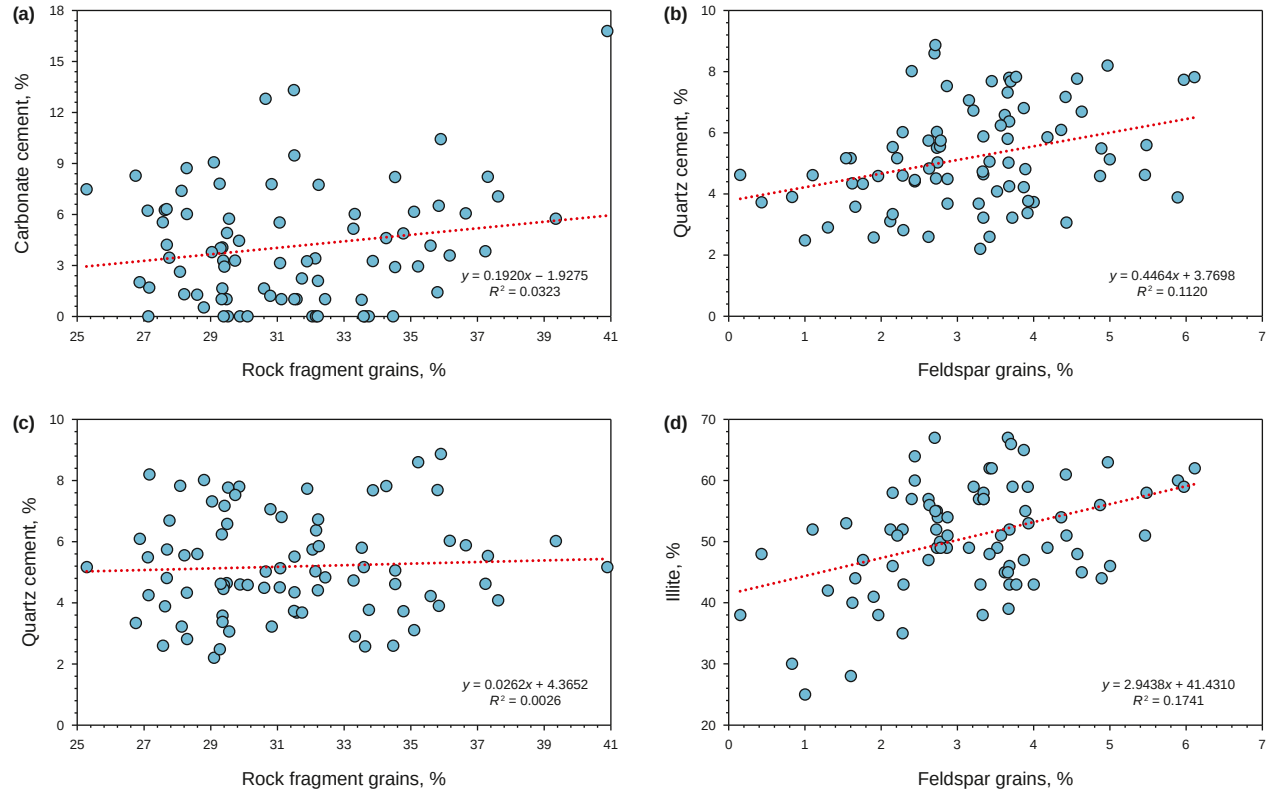

Fig. 15. Relationship between authigenic mineral content and detrital grain content in the Xu3 sandstone reservoirs. The illite content is the relative content of clay minerals, whereas the other contents use the absolute content.

sandstone pores were acidic organic fluids. These acidic fluids further engaged in dissolution reactions with feldspar and rock fragment particles (Fig. 16), generating dissolution by-products that stimulated the growth of SiO_2 and kaolinite (Ma et al., 2017). With the development of diagenesis, diagenetic fluids within the pore space gradually transitioned from acidic to alkaline environments (Dutton, 2008). In alkaline settings, substantial amounts of alkali metal ions combined with CO_2 and CO_3^{2-} in the fluids to precipitate and form ferro-calcite and ankerite (Fig. 7(b), (h), and (i)). In alkaline environments, the presence of abundant alkali metals in diagenetic fluids can promote the generation of clay minerals such as illite and chlorite (Fig. 10(b)–(d)) (Bjørlykke and Jahren, 2012; Xi et al., 2019). During the mesodiagenetic stage, elevated stratigraphic temperatures led to the illiticization of potassium feldspar, resulting in the formation of illite (Fig. 10(b)), whereas chloritization of kaolinite led to the formation of chlorite (Fig. 10(d)) (Bloch et al., 2002; Oluwadebi et al., 2018). Microscopic observations revealed the dense characteristics of

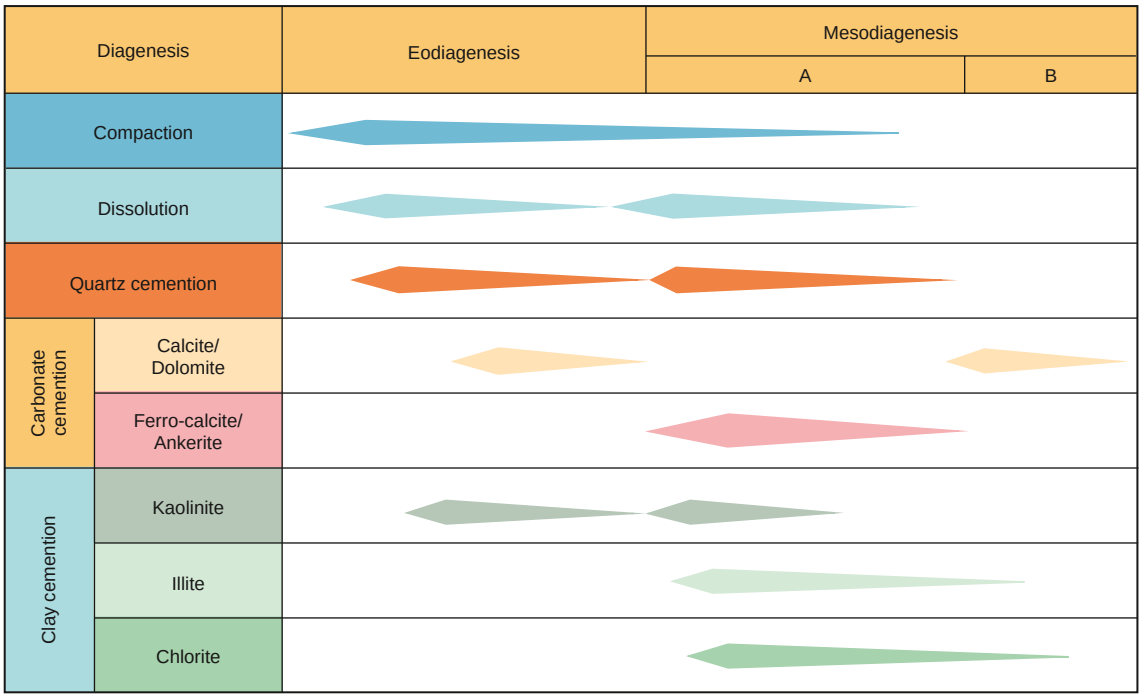

Fig. 16. Characteristics of diagenetic sequence in the Xu3 tight sandstone.

sandstone reservoirs cut by fractures (Fig. 7(c)). Additionally, the measured peak temperature distribution of the fluid inclusion homogenization temperatures in calcite within the fracture was approximately 130 °C (Fig. 12(d)). This suggested that carbonate cement filling the fracture formed during the latter part of the mesodiagenetic stage (Fig. 16) (Chen et al., 2016).

5.3. Diagenesis controls reservoir quality

Reservoir quality typically refers to the porosity and permeability of the reservoir (Liu and Xiong, 2021; Xi et al., 2019), and is influenced by sedimentation and diagenesis processes, including particle sorting, particle size distribution, compaction, cementation, and dissolution (Oluwadebi et al., 2018; Schmid et al., 2004). The contact relationships of detrital particles (Fig. 5(a) and (c)) and various types of cement (Figs. 7 and 11) suggest a pronounced effect of compaction and cementation on the reservoir quality of the Xu3 Member in the study area. A plot illustrating the relationship between IGV and cement volume in the Xu3 Member's tight sandstone reservoirs is shown in Fig. 6. Approximately 12.4% of the samples showed porosity reduction, mainly attributed to cementation, whereas 87.6% were predominantly affected by compaction (Houseknecht, 1987). This indicates that in the study area, the properties of the Xu3 sandstone reservoirs are predominantly influenced by compaction, with local control by cementation (Adepehin et al., 2020).

Diagenesis, influenced by its impact on reservoir quality, is commonly categorized as destructive or constructive (Liu et al., 2014; Xu et al., 2023). In sandstone reservoirs, compaction and cementation effects can exemplify destructive diagenesis (Oluwadebi et al., 2018). Dissolution represents constructive diagenesis (Mansurbeg et al., 2008). Petrographic observations revealed that the sandstone reservoirs in the research stratigraphic member of the study area were characterized by the development of dissolution porosity (Fig. 5(d) and (e)). Analysis of the relationship between physical data and clastic particle content demonstrated a positive correlation between porosity and permeability and the presence of easily dissolved particles (Fig. 17(a)–(d)), along with a negative correlation with the quartz particle content (Fig. 17(e) and (f)). This suggested that the dissolution process enhanced reservoir quality by creating pore spaces through the dissolution of feldspar and rock fragment particles.

The dissolution of particles facilitates the generation of secondary pores and concurrently promotes the development of authigenic minerals (Leitner et al., 2020). The quartz and clay minerals that developed during diagenesis primarily originated from dissolution. Consequently, the physical properties of the reservoir were positively correlated with these two authigenic minerals (Fig. 18(a)–(d)). Carbonate cement formation originates not only via the dissolution of internal particles but also from adjacent mudstone layers and hydrothermal activity in the deeper parts of the formation. Both internal and external sources contribute to carbonate cementation in the stratigraphic member of the study area, resulting in increased pore space occupation and reservoir densification (Liu and Xiong, 2021;Ma et al., 2017). Consequently, a negative correlation exists between the carbonate cement content and physical properties of the reservoir (Fig. 18(e) and (f)). The preceding analysis indicated that diagenesis notably altered the quality of the reservoirs in the stratigraphic member within the depression zone. Compaction, dissolution, and carbonate cementation exerted a significant influence on the physical properties of reservoirs.

5.4. Implication for reservoir heterogeneity

Sandstone reservoir heterogeneity primarily stems from sedimentary facies in paleo-sedimentary environments (Liu et al., 2018b). During the diagenetic stage, dissolution and cementation modify reservoirs, typically intensifying their heterogeneity (Morad et al., 2010; Shi et al., 2017). Within the stratigraphic member, the sandstone body of the reservoir, under the influence of sedimentary facies, typically exhibits a positive cycle type,

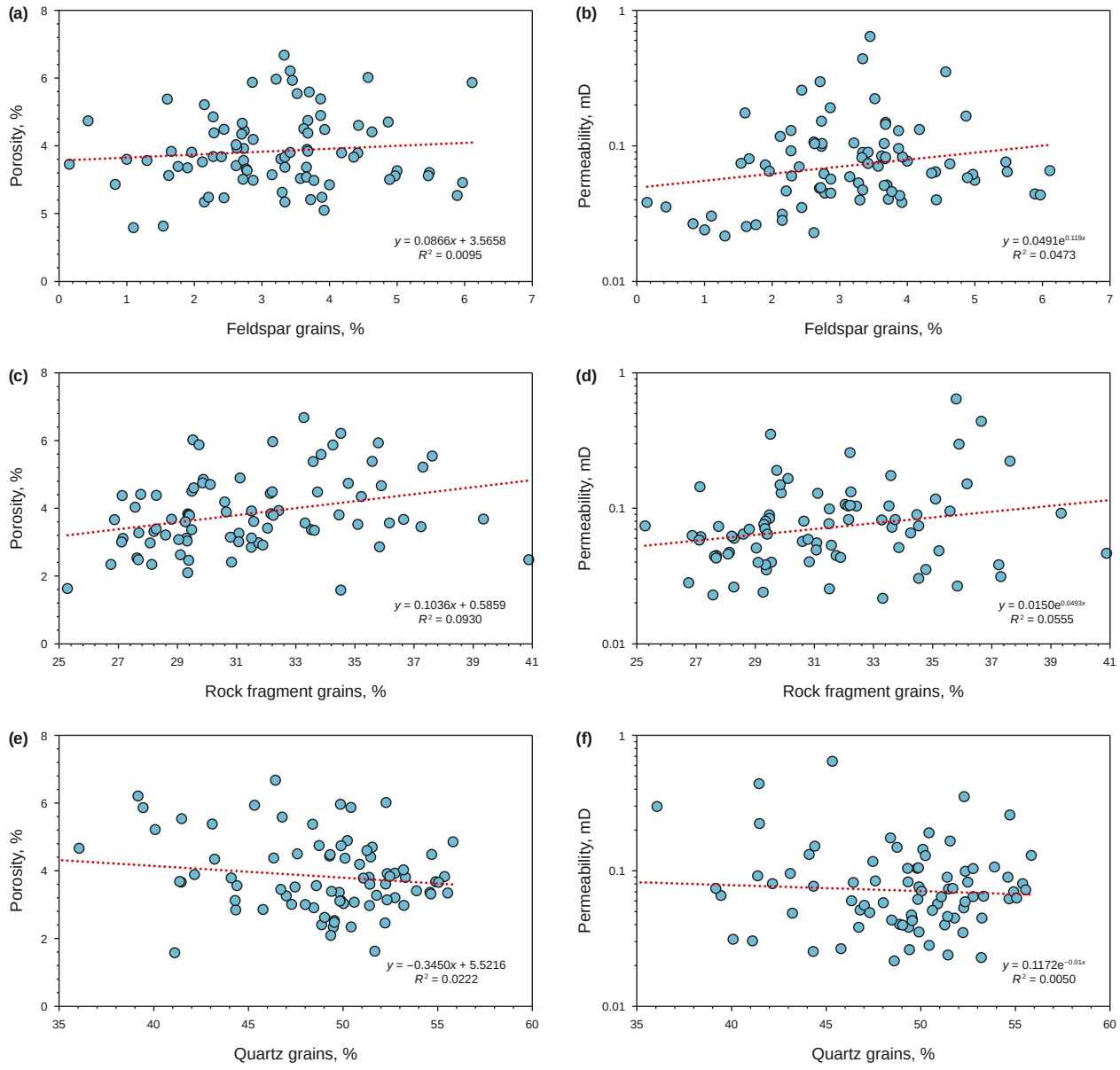

Fig. 17. Relationships between detrital grains and reservoir quality of Xu3 sandstone reservoirs. The detrital grain content used the absolute content.

characterized by larger grain sizes at the bottom and smaller ones at the top (Figs. 19(a) and 20(a)). These sandstone bodies can be categorized into two overlaying styles: sandstone overlaying sandstone (SOS) (Fig. 19(b)) and mudstone overlaying sandstone (MOS) (Fig. 20(b)). By examining these two vertical combinations of sandstone bodies, we assessed the impact of diagenesis on the heterogeneity of tight sandstone reservoirs in the depression zone of a foreland basin.

5.4.1. SOS style

The SOS style comprises two overlaying positive cycles, with the upper cycle comprising siltstone and fine sandstone and the lower cycle consisting of fine sandstone. The grain size of the sandstone gradually decreased from the bottom to the top of each cycle (Fig. 19). According to the previous analysis, the sandstone reservoirs of the stratigraphic member of the study area underwent two phases of diagenetic modification by organic acidic fluids (Fig. 16). Given that sandstone grains were coarse at the bottom and fine at the top of each cycle, pore-throat conditions were better in the lower part, leading to the predominant migration of diagenetic fluid along this region (Fig. 19(b)) (Kadkhodaie et al., 2021; Luo et al., 2022). Thus, these conditions lead to more pronounced dissolution occurring at the base. Vertically, the dissolution effect progressively diminishes. Consequently, dissolution-induced pores mainly develop at the base, where easily dissolvable particles (feldspars and rock fragment particles) react with the dissolution fluid in abundance, releasing numerous ions into the diagenetic fluid (Ma et al., 2017; Taylor et al., 2010). The high ionic content of the bottom diagenetic fluid allows ions to migrate both horizontally and vertically, driven by concentration disparities (Ahmed, 2002; Worden and Morad, 2000). SiO_2 transport is weak in the vertical direction, whereas K^+, Ca^{2+}, and Mg^{2+} exhibit transport capabilities (Liu and Xiong, 2021; Stroker et al., 2013; Xi et al., 2015). Variances in the ion vertical transport capacity resulted in quartz cement predominantly developing in the lower part of the cycle, whereas carbonate cement and clay

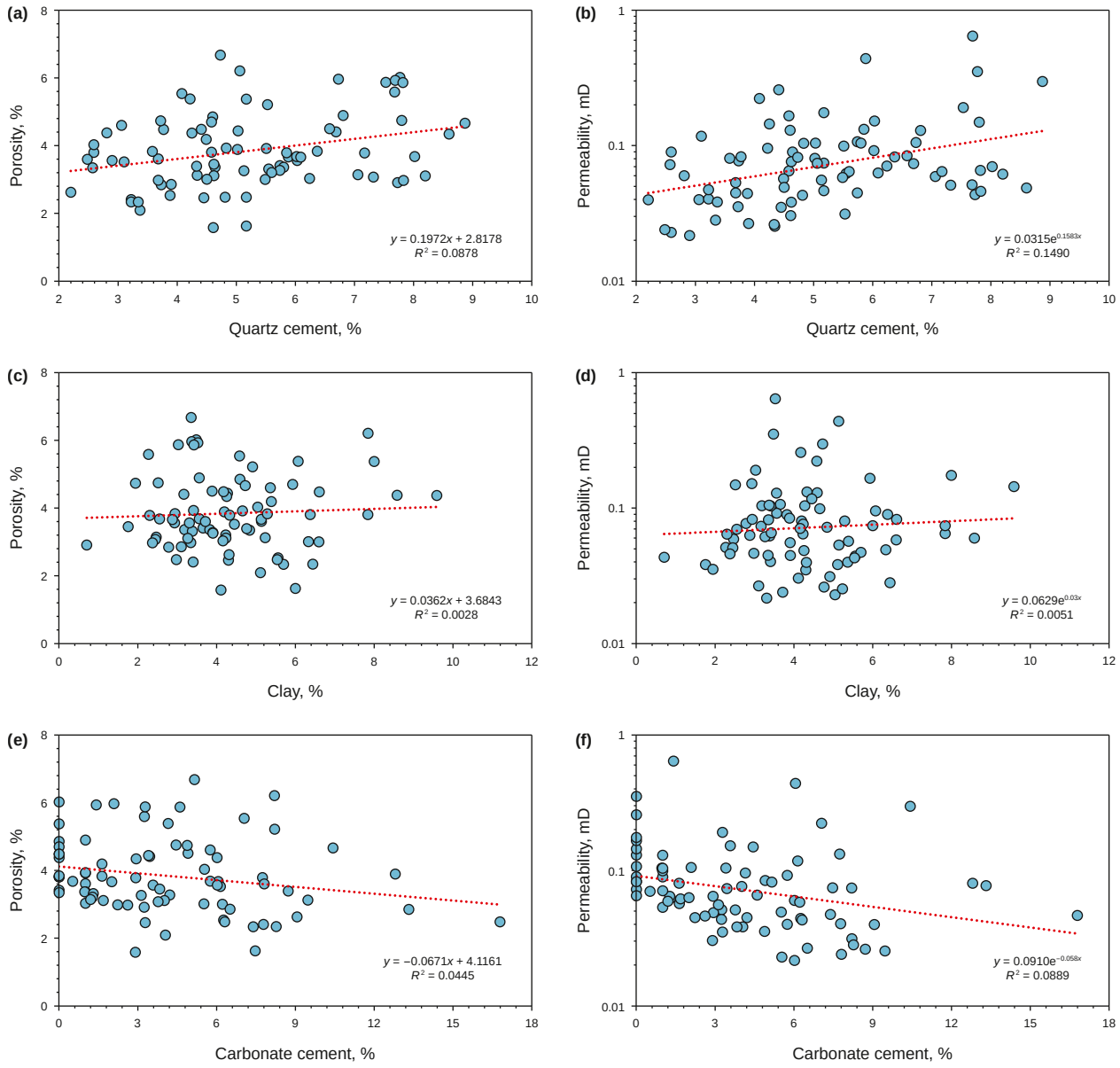

Fig. 18. Relationships between authigenic minerals and reservoir quality of Xu3 sandstone reservoirs. The authigenic mineral content used the absolute content.

cement primarily developed in the central and top parts (Fig. 19(b)).

5.4.2. MOS style

The MOS style is characterized by a vertical sequence of sandstones in the lower segment and mudstones in the upper segment, exhibiting a gradual fining of grain size from bottom to top (Fig. 20(a)). The pore-throat conditions remained superior in the lower segment, influenced by two periods of acidic diagenetic fluids primarily conveyed along the base (Fig. 20(b)). Additionally, the presence of mudstone at the top of the cycle facilitated the direct injection of organic acids from above into the sandstone (Fig. 20(b)) (Liu and Xiong, 2021; Luo et al., 2022). Hence, the dissolution was more pronounced at the top and base of the sandstone, with minimal dissolution observed in the central region. This resulted in the primary development of secondary dissolution porosity at these locations. Hence, the reservoir predominantly formed at the top and base extremities of the sandstone body in the MOS style (Fig. 20(b)). This scenario prompted dissolvable particles to react extensively with dissolution fluids at the top and bottom of the cycle, liberating numerous ions into diagenetic fluids that were transported both vertically and horizontally driven by concentration gradients. Vertically, varying ion transport capacities led to the formation of quartz cement in the top and bottom sandstones of the cycle, whereas carbonate and clay cement distributions predominated in the central region (Fig. 20(b)).

The diagenesis strongly influenced the two sandstone overlay styles within the stratigraphic member of the study area. Vertically, various types of authigenic minerals exhibited distinct distributions, and the distribution of the secondary dissolution porosity differed between the two overlay types, significantly contributing to the heterogeneity of the sandstone reservoir. Within the foreland basin depression zone, high-quality tight sandstone reservoirs exhibited varying distributions across different sandstone overlay types. Notably, high-quality tight

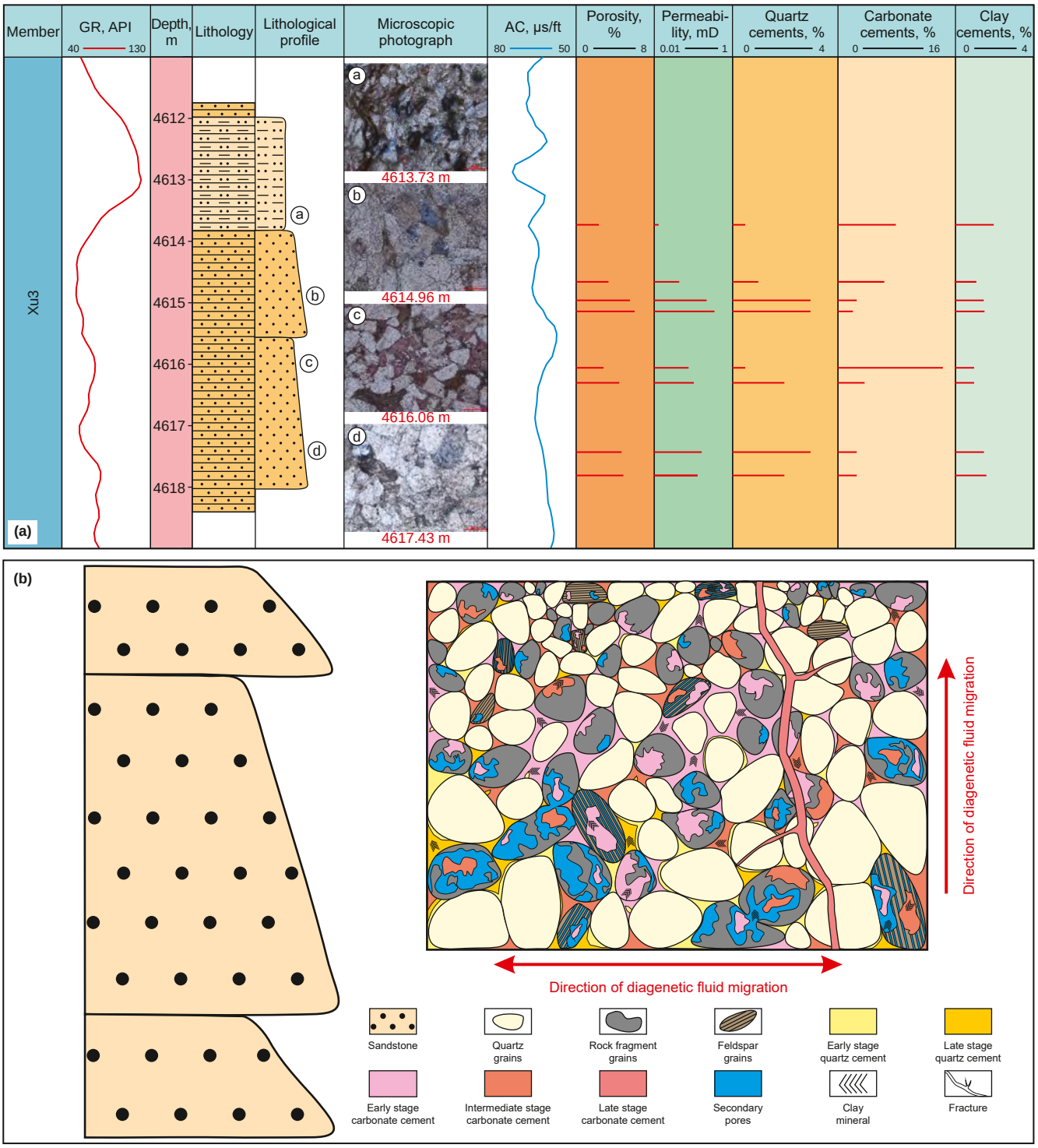

Fig. 19. **(a)** Characteristics of physical properties and authigenic mineral development of two positively cyclic sandstones with vertical overlap, Well DY2. **(b)** Diagenetic features and distribution of relatively high-quality reservoirs in the sandstone-overlain sandstone style.

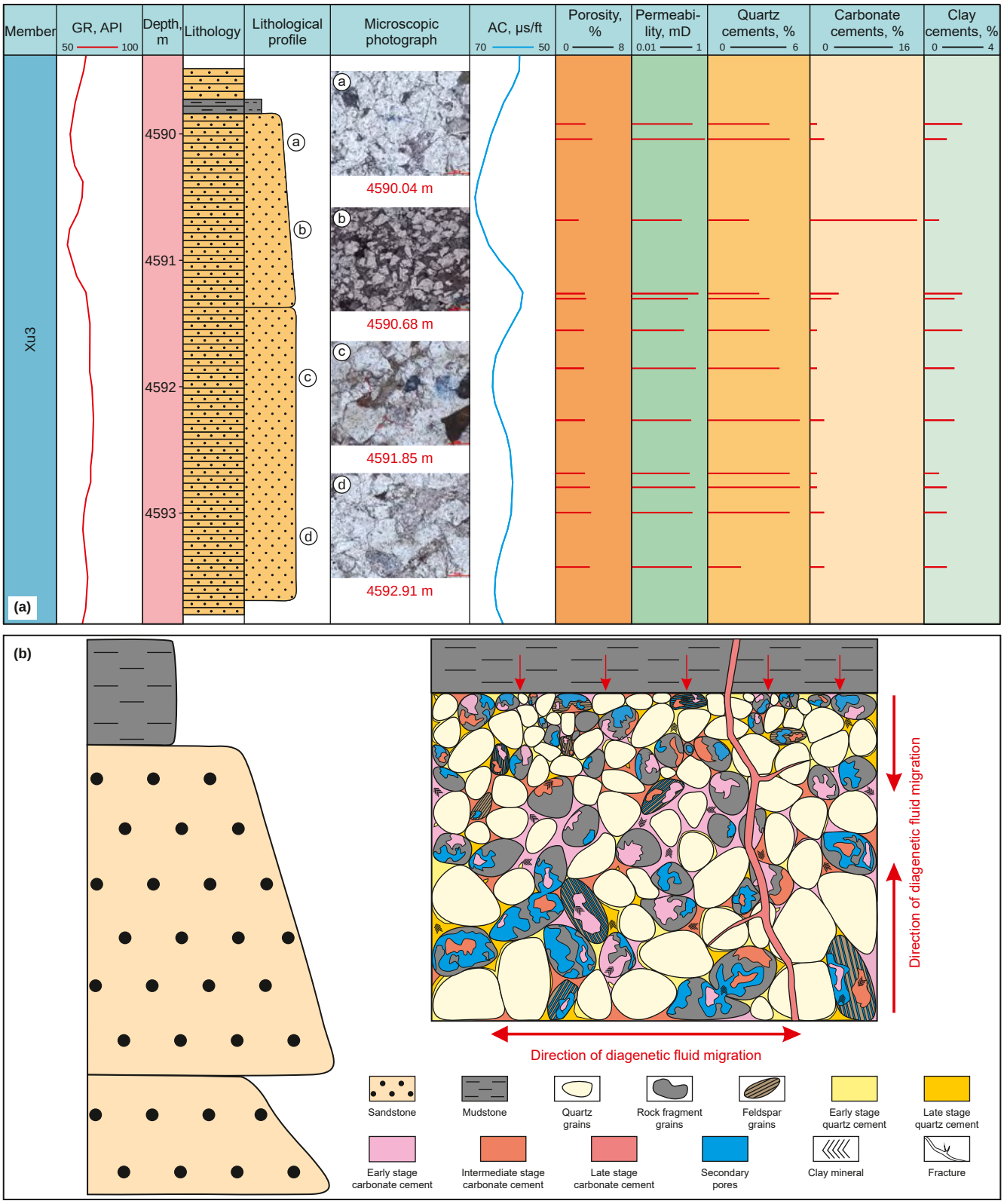

Fig. 20. **(a)** Development of mudstones at the top of sandstones in a vertically positive cycle, along with the physical characteristics and authigenic mineral development of the sandstones, Well DY102. **(b)** Diagenetic features and distribution of relatively high-quality reservoirs in the mudstone-overlain sandstone style.

sandstone reservoirs mainly developed at the base of the SOS style (Fig. 19(b)). Conversely, in the MOS style, high-quality reservoirs were observed at the base and top of sandstone (Fig. 20(b)).

6. Conclusions

(1) The lithology of tight sandstone reservoirs consisted predominantly of sublitharenite and litharenite, characterized by medium to fine grain sizes and moderate sorting.
(2) Tight sandstone exhibited relatively poor physical properties, with a positive correlation between porosity and permeability. The average porosity was 3.82%, and the average permeability was 0.1 mD.
(3) The tight sandstone reservoirs were modified by several diagenetic events including compaction, dissolution, carbonate cementation, quartz cementation, and clay cementation.
(4) The tight sandstone reservoir featured three stages of carbonate cement development. Organic matter maturation and dissolution facilitated the ESCC and ISCC, whereas hydrothermal activity drove the formation of the LSCC.
(5) Two stages of quartz cement development were evident in tight sandstone reservoirs. This mechanism involves the dissolution of feldspar grains by organic acidic fluids and the subsequent transformation of clay minerals.
(6) In the eodiagenetic stage, authigenic minerals, such as ESCC (calcite, dolomite), early-stage quartz cement, and kaolinite, were formed. In the mesodiagenetic stage, the formation of authigenic minerals included ISCC and LSCC (ferro-calcite, ankerite, and calcite in fractures), late-stage quartz cement, and clay cement (kaolinite, illite, and chlorite).
(7) In reservoirs, compaction and cementation were the primary destructive diagenetic processes, with compaction having a more detrimental effect on the reservoir quality than cementation. Conversely, dissolution served as the principal constructive diagenetic process in the reservoir, promoting cementation.
(8) Diagenesis contributed to the increased heterogeneity of sandstone reservoirs across the two overlay types. In the SOS style, high-quality reservoirs primarily developed at the bottom of the cycle, whereas in the MOS style, they were identified at both the top and bottom of the sandstone within the cycle. This study enhances the understanding of tight sandstone reservoirs in depressions of foreland basins and supports the exploration and development of hydrocarbons in similar geological settings worldwide.

CRediT authorship contribution statement

Peng Huang: Writing – review & editing, Writing – original draft, Visualization, Formal analysis. **Ming-Jie Liu:** Writing – review & editing, Project administration, Funding acquisition, Data curation, Conceptualization. **Bo Cao:** Writing – review & editing, Validation, Methodology. **Zi-Long Wang:** Writing – review & editing, Investigation.

Data availability

The data will be made available upon request.

Declaration of competing interest

The authors declare that they have no known competing financial interests or personal relationships that could have appeared to influence the work reported in this paper.

Acknowledgements

This study was funded by the Natural Science Foundation of China (Grant No. 41872154) and Sinopec Science and Technology Department Project (Grant No. P20061-3). We express our gratitude to the Sinopec Southwest Oil & Gas Company for supplying the samples and the geological information. We are grateful for the assistance Professor Fei Li at Southwest Petroleum University for the analysis of the carbon and oxygen isotopes, as well as the in situ rare earth elements. We appreciate the time and work put forward by the editor and reviewers.

Supplementary data

Supplementary data to this article can be found online at https://doi.org/10.1016/j.petsci.2025.12.016.

References

Adepehin, E.J., Ali, C.A., Zakaria, A.A., et al., 2020. Post-depositional controls on siliciclastic tight reservoirs: implications from the Oligocene nyalau formation (cycle 1), onshore central Sarawak, Borneo. Mar. Petrol. Geol. 111, 786–806. https://doi.org/10.1016/j.marpetgeo.2019.09.004.
Ahmed, W., 2002. Diagenesis and mass transfer between permo-triassic sandstones and interbedded mudstones, Ulster Basin. Bull. Chem. Soc. Ethiop. 16 (1), 9–35. https://doi.org/10.4314/bcse.v16i1.20946.
Baytok, S., Pranter, M.J., 2013. Fault and fracture distribution within a tight-gas sandstone reservoir: Mesaverde group, mamm creek field, Piceance Basin, Colorado, USA. Pet. Geosci. 19 (3), 203–222. https://doi.org/10.1144/petgeo2011-093.
Bjørlykke, K., Jahren, J., 2012. Open or closed geochemical systems during diagenesis in sedimentary basins: Constraints on mass transfer during diagenesis and the prediction of porosity in sandstone and carbonate reservoirs. AAPG Bull. 96 (12), 2193–2214. https://doi.org/10.1306/04301211139.
Blake, R.E., Walter, L.M., 1999. Kinetics of feldspar and quartz dissolution at 70–80°C and near-neutral pH: Effects of organic acids and NaCl. Geochim. Cosmochim. Acta 63 (13–14), 2043–2059. https://doi.org/10.1016/S0016-7037(99)00072-1.
Bloch, S., Lander, R.H., Bonnell, L., 2002. Anomalously high porosity and permeability in deeply buried sandstone reservoirs: origin and predictability. AAPG Bull. 86 (2), 301–328. https://doi.org/10.1306/61EEDABC-173E-11D7-8645000102C1865D.
Boettcher, D.J., Thomas, M., Hrudey, M.G., et al., 2010. The Western Canada foreland basin: A basin-centred gas system. Petrol. Geol. Conf. Seri. 7, 1099–1123. https://doi.org/10.1144/0071099.
Bojanowski, M.J., 2014. Authigenic dolomites in the Eocene–Oligocene organic carbon-rich shales from the Polish outer carpathians: Evidence of past gas production and possible gas hydrate formation in the Silesian Basin. Mar. Petrol. Geol. 51, 117–135. https://doi.org/10.1016/j.marpetgeo.2013.12.001.
Chen, C., Xu, G., Xu, F., et al., 2016. Sequence of densification and hydrocarbon charging of Xu2 reservoir in anyue–Hechuan area, Sichuan Basin, China. J. Cent. South Univ. 23 (6), 1439–1448. https://doi.org/10.1007/s11771-016-3196-8.
Chen, S., Yang, Y., Qiu, L., et al., 2024. Source of quartz cement and its impact on reservoir quality in Jurassic Shaximiao Formation in central Sichuan Basin. China. Mar. Petrol. Geol. 159, 106543. https://doi.org/10.1016/j.marpetgeo.2023.106543.
Debruyne, D., Hulsbosch, N., Muchez, P., 2016. Unraveling rare earth element signatures in hydrothermal carbonate minerals using a source–sink system. Ore Geol. Reviews 72, 232–252. https://doi.org/10.1016/j.oregeorev.2015.07.022.
Deng, J., Liu, M., Ji, Y., et al., 2022. Controlling factors of tight sandstone gas accumulation and enrichment in the slope zone of foreland basins: The Upper Triassic Xujiahe Formation in Western Sichuan foreland basin, China. J. Pet. Sci. Eng. 214, 110474. https://doi.org/10.1016/j.petrol.2022.110474.
Denny, A.C., Kozdon, R., Kitajima, K., et al., 2017. Isotopically zoned carbonate cements in early Paleozoic sandstones of the Illinois basin: $\delta^{18}O$ and $\delta^{13}C$ records of burial and fluid flow. Sediment. Geol. 361, 93–110. https://doi.org/10.1016/j.sedgeo.2017.09.004.
Desbois, G., Urai, J.L., Kukla, P.A., et al., 2011. High-resolution 3D fabric and porosity model in a tight gas sandstone reservoir: A new approach to investigate microstructures from mm- to nm-scale combining argon beam cross-sectioning and SEM imaging. J. Pet. Sci. Eng. 78 (2), 243–257. https://doi.org/10.1016/j.petrol.2011.06.004.
Dutton, S.P., 2008. Calcite cement in Permian deep-water sandstones, Delaware Basin, west Texas: Origin, distribution, and effect on reservoir properties. AAPG Bull. 92 (6), 765–787. https://doi.org/10.1306/01280807107.
Dutton, S.P., Loucks, R.G., 2010. Reprint of: Diagenetic controls on evolution of porosity and permeability in lower tertiary wilcox sandstones from shallow to ultradeep (200–6700 m) burial, Gulf of Mexico Basin. USA Mar. Petrol. Geol. 27 (1), 69–81. https://doi.org/10.1016/j.marpetgeo.2009.08.008.

Fayek, M., Harrison, T.M., Grove, M., et al., 2001. In situ stable isotopic evidence for protracted and complex carbonate cementation in a petroleum reservoir, north coles levee, San Joaquin Basin, California. USA J. Sediment. Res. 71 (3), 444–458. https://doi.org/10.1306/2DC40954-0E47-11D7-8643000102C1865D.
Fic, J., Pedersen, P.K., 2013. Reservoir characterization of a "tight" oil reservoir, the middle Jurassic upper shaunavon member in the whitemud and eastbrook pools, SW Saskatchewan. Mar. Petrol. Geol. 44, 41–59. https://doi.org/10.1016/j.marpetgeo.2013.03.013.
Folk, R.L., 1980. Petrology of sedimentary rocks. Hemphill Publishing Company, Austin, Texas, p. 182.
Gardner, J., Wheeler, J., Mariani, E., 2021. Interactions between deformation and dissolution-precipitation reactions in plagioclase feldspar at greenschist facies. Lithos 396–397, 106241. https://doi.org/10.1016/j.lithos.2021.106241.
Gier, S., Worden, R.H., Johns, W.D., et al., 2008. Diagenesis and reservoir quality of Miocene sandstones in the Vienna Basin, Austria. Mar. Petrol. Geol. 25 (8), 681–695. https://doi.org/10.1016/j.marpetgeo.2008.06.001.
Giles, M.R., de Boer, R.B., 1990. Origin and significance of redistributional secondary porosity. Mar. Petrol. Geol. 7 (4), 378–397. https://doi.org/10.1016/0264-8172(90)90016-A.
Gong, L., Zeng, L., Gao, Z., et al., 2016. Reservoir characterization and origin of tight gas sandstones in the Upper Triassic Xujiahe Formation, Western sichuan Basin, China. J. Petrol. Explor. Prod. Technol. 6, 319–329. https://doi.org/10.1007/s13202-015-0203-9.
Grundtner, M.-L., Gross, D., Gratzer, R., et al., 2017. Carbonate cementation in upper Eocene clastic reservoir rocks from the North Alpine Foreland Basin (Austria). Austrian J. Earth Sci 110 (1). https://doi.org/10.17738/ajes.2017.0005.
Guo, T., 2013. Key controls on accumulation and high production of large non-marine gas fields in northern Sichuan Basin. Petrol. Explor. Dev. 40 (2), 150–160. https://doi.org/10.1016/S1876-3804(13)60018-X.
Hao, F., Guo, T., Zhu, Y., et al., 2008. Evidence for multiple stages of oil cracking and thermochemical sulfate reduction in the puguang gas field, Sichuan Basin, China. AAPG Bull, 92 (5), 611–637. https://doi.org/10.1306/01210807090.
Houseknecht, D.W., 1987. Assessing the relative importance of compaction processes and cementation to reduction of porosity in Sandstones1. AAPG Bull. 71 (6), 633–642. https://doi.org/10.1306/9488787F-1704-11D7-8645000102C1865D.
Hyodo, A., Kozdon, R., Pollington, A.D., et al., 2014. Evolution of quartz cementation and burial history of the eau claire formation based on in situ oxygen isotope analysis of quartz overgrowths. Chem. Geol. 384, 168–180. https://doi.org/10.1016/j.chemgeo.2014.06.021.
Imin, A., Zha, M., Ding, X., et al., 2020. Identification of a Permian foreland basin in the Western Junggar Basin (NW China) and its impact on hydrocarbon accumulation. J. Pet. Sci. Eng. 187, 106810. https://doi.org/10.1016/j.petrol.2019.106810.
Jiang, Z., Ran, B., Li, Z., et al., 2023. A Late Triassic depositional age for the Xujiahe Formation, Sichuan Basin: Implications for the closure of the paleo-tethys ocean. Mar. Petrol. Geol. 155, 106346. https://doi.org/10.1016/j.marpetgeo.2023.106346.
Jin, X., Shi, Z., Rigo, M., et al., 2018. Carbonate platform crisis in the Carnian (Late Triassic) of Hanwang (Sichuan Basin, south China): Insights from conodonts and stable isotope data. J. Asian Earth Sci. 164, 104–124. https://doi.org/10.1016/j.jseaes.2018.06.021.
Kadkhodaie, R., Kadkhodaie, A., Rezaee, R., 2021. Study of pore system properties of tight gas sandstones based on analysis of the seismically derived velocity deviation log: A case study from the Perth Basin of western Australia. J. Pet. Sci. Eng. 196, 108077. https://doi.org/10.1016/j.petrol.2020.108077.
Kordi, M., 2019. Sedimentary basin analysis of the neo-tethys and its hydrocarbon systems in the southern zagros fold-thrust belt and foreland basin. Earth Sci. Rev. 191, 1–11. https://doi.org/10.1016/j.earscirev.2019.02.005.
Lai, J., Wang, G., Chen, J., et al., 2017. Origin and distribution of carbonate cement in tight sandstones: the Upper Triassic Yanchang Formation chang 8 oil layer in west Ordos Basin, China. Geofluids 2017 (1), 8681753. https://doi.org/10.1155/2017/8681753.
Lai, J., Wang, G., Cai, C., et al., 2018. Diagenesis and reservoir quality in tight gas sandstones: The fourth member of the Upper Triassic Xujiahe Formation, central Sichuan Basin, Southwest China. Geol. J. 53 (2), 629–646. https://doi.org/10.1002/gj.2917.
Law, B.E., Curtis, J.B., 2002. Introduction to unconventional petroleum systems. AAPG Bull. 86 (11), 1851–1852. https://doi.org/10.1306/61EEDDA0-173E-11D7-8645000102C1865D.
Lee, S.-G., Lee, D.-H., Kim, Y., et al., 2003. Rare earth elements as indicators of groundwater environment changes in a fractured rock system: Evidence from fracture-filling calcite. Appl. Geochem. 18 (1), 135–143. https://doi.org/10.1016/S0883-2927(02)00071-9.
Leitner, C., Gross, D., Friedl, G., et al., 2020. Sandstone diagenesis in a halite deposit, from surface to high-grade diagenesis (Haselgebirge formation, Eastern alps). Sediment. Geol. 399, 105614. https://doi.org/10.1016/j.sedgeo.2020.105614.
Li, Z., Jia, D., Chen, W., 2013. Structural geometry and deformation mechanism of the longquan anticline in the longmen Shan fold-and-thrust belt, Eastern Tibet. J. Asian Earth Sci. 64, 223–234. https://doi.org/10.1016/j.jseaes.2012.12.022.
Li, Y., Shao, L., Eriksson, K.A., et al., 2014. Linked sequence stratigraphy and tectonics in the Sichuan Continental foreland basin, Upper Triassic Xujiahe Formation, southwest China. J. Asian Earth Sci. 88, 116–136. https://doi.org/10.1016/j.jseaes.2014.02.025.
Li, H., Tang, H., Qin, Q., et al., 2019a. Characteristics, formation periods and genetic mechanisms of tectonic fractures in the tight gas sandstones reservoir: A case study of Xujiahe Formation in YB area, Sichuan Basin, China. J. Pet. Sci. Eng. 178, 723–735. https://doi.org/10.1016/j.petrol.2019.04.007.
Li, M., Zhu, R., Lou, Z., et al., 2019b. Diagenesis and its impact on the reservoir quality of the fourth member of xujiahe Formation, Western Sichuan depression, China. Mar. Petrol. Geol. 103, 485–498. https://doi.org/10.1016/j.marpetgeo.2019.03.011.
Li, Y., Chen, S., Qiu, W., et al., 2019c. Controlling factors for the accumulation and enrichment of tight sandstone gas in the Xujiahe Formation, Guang'an area, Sichuan Basin. Energy Explor. Exploit. 37 (1), 26–43. https://doi.org/10.1177/0144598718803224.
Lin, M., Wang, Y., Cao, Y., et al., 2020. Sources of Ca^{2+} in the major carbonate cements in Eocene sandstones and conglomerates: Evidence from Sr isotopes, Sr/Ca ratios, and rare-earth elements. Mar. Petrol. Geol. 120, 104568. https://doi.org/10.1016/j.marpetgeo.2020.104568.
Liu, S., Deng, B., Li, Z., et al., 2012. Architecture of basin-mountain systems and their influences on gas distribution: A case study from the Sichuan Basin, South China. J. Asian Earth Sci. 47, 204–215. https://doi.org/10.1016/j.jseaes.2011.10.012.
Liu, M., Liu, Z., Sun, X., et al., 2014. Paleoporosity and critical porosity in the accumulation period and their impacts on hydrocarbon accumulation—A case study of the middle Es3 member of the Paleogene Formation in the niuzhuang sag, dongying depression, Southeastern Bohai Bay Basin, East China. Pet. Sci. 11 (4), 495–507. https://doi.org/10.1007/s12182-014-0365-y.
Liu, Y., Qiu, N., Xie, Z., et al., 2016. Overpressure compartments in the central paleo-uplift, Sichuan Basin, Southwest China. AAPG Bull. 100 (5), 867–888. https://doi.org/10.1306/02101614037.
Liu, J., Liu, K., Jiang, Z., et al., 2018a. Hydrocarbon accumulation processes in the Yangtake Foldbelt, Kuqa Foreland Basin, NW China: Insights from integrated basin modelling and fluid inclusion analyses. J. Pet. Geol. 41 (4), 447–466. https://doi.org/10.1111/jpg.12716.
Liu, Y., Hu, W., Cao, J., et al., 2018b. Diagenetic constraints on the heterogeneity of tight sandstone reservoirs: A case study on the Upper Triassic Xujiahe formation in the Sichuan basin, Southwest China. Mar. Petrol. Geol. 92, 650–669. https://doi.org/10.1016/j.marpetgeo.2017.11.027.
Liu, Y., Hu, W., Cao, J., et al., 2019. Fluid–rock interaction and its effects on the Upper Triassic tight sandstones in the Sichuan Basin, China: Insights from petrographic and geochemical study of carbonate cements. Sediment. Geol. 383, 121–135. https://doi.org/10.1016/j.sedgeo.2019.01.012.
Liu, M., Xiong, C., 2021. Diagenesis and reservoir quality of deep-lacustrine sandy-debris-flow tight sandstones in Upper Triassic Yanchang Formation, Ordos Basin, China: Implications for reservoir heterogeneity and hydrocarbon accumulation. J. Pet. Sci. Eng. 202, 108548. https://doi.org/10.1016/j.petrol.2021.108548.
Liu, J., Li, L., Zhang, C., et al., 2022. Identification and quantitative evaluation of pores and throats of a tight sandstone reservoir (Upper Triassic Xujiahe Formation, Sichuan Basin, China). Mar. Petrol. Geol. 140, 105663. https://doi.org/10.1016/j.marpetgeo.2022.105663.
Liu, J., Yang, X., Liu, K., et al., 2023a. Differential hydrocarbon generation and evolution of typical terrestrial gas-prone source rocks: an example from the kuqa foreland basin, NW China. Mar. Petrol. Geol. 152, 106225. https://doi.org/10.1016/j.marpetgeo.2023.106225.
Liu, Z., Wu, S., Xu, Z., et al., 2023b. Impact of coal evolution on formation of tight sandstone reservoirs: a case study in the Daniudi gas field, ordos basin, China. Energy Explor. Exploit. 41, 1576–1602. https://doi.org/10.1177/01445987231178561.
Longstaffe, F.J., Calvo, R., Ayalon, A., et al., 2003. Stable isotope evidence for multiple fluid regimes during carbonate cementation of the upper tertiary hazeva formation, dead sea graben, southern Israel. J. Geochem. Explor. 80 (2–3), 151–170. https://doi.org/10.1016/S0375-6742(03)00189-4.
Lu, F., Tan, X., Xiao, D., et al., 2023a. Sedimentary control on diagenetic paths of dolomite reservoirs in a volcanic setting: a case study of the Permian Chihsia formation in the Sichuan basin, China. Sediment. Geol. 454, 106451. https://doi.org/10.1016/j.sedgeo.2023.106451.
Lu, G., Chen, X., Zou, H., et al., 2023b. Provenance of the first terrigenous sediments in the western Sichuan basin during the Late Triassic: implications for basin evolution from marine to continental. Mar. Petrol. Geol. 147, 105992. https://doi.org/10.1016/j.marpetgeo.2022.105992.
Luo, L., Jia, D., Qi, J., et al., 2013. Tectono–sedimentary evolution of the Late Triassic Xujiahe Formation in the Sichuan Basin. Acta Geol. Sin. 87 (6), 1554–1568. https://doi.org/10.1111/1755-6724.12159.
Luo, L., Meng, W., Gluyas, J., et al., 2019. Diagenetic characteristics, evolution, controlling factors of diagenetic system and their impacts on reservoir quality in tight deltaic sandstones: Typical example from the Xujiahe Formation in Western Sichuan Foreland Basin, SW China. Mar. Petrol. Geol. 103, 231–254. https://doi.org/10.1016/j.marpetgeo.2019.02.012.
Luo, C., Chen, X., Shi, Z., et al., 2022. Effects of precipitation and dissolution of carbonate cements on the quality of deeply buried high-temperature and overpressured clastic reservoirs: XD 10 block, Yinggehai Basin, South China Sea. Mar. Petrol. Geol. 139, 105591. https://doi.org/10.1016/j.marpetgeo.2022.105591.
Ma, Y., Guo, X., Guo, T., et al., 2007. The puguang gas field: New giant discovery in the mature Sichuan Basin, Southwest China. AAPG Bull. 91 (5), 627–643. https://doi.org/10.1306/11030606062.
Ma, B., Cao, Y., Jia, Y., 2017. Feldspar dissolution with implications for reservoir quality in tight gas sandstones: Evidence from the Eocene Es4 interval,

Dongying depression, Bohai Bay Basin, China. J. Pet. Sci. Eng. 150, 74–84. https://doi.org/10.1016/j.petrol.2016.11.026.
Ma, B., Liang, H., Wu, G., et al., 2023. Formation and evolution of the strike-slip faults in the central Sichuan Basin, SW China. Petrol. Explor. Dev. 50 (2), 373–387. https://doi.org/10.1016/S1876-3804(23)60394-5.
Mansurbeg, H., Morad, S., Salem, A., et al., 2008. Diagenesis and reservoir quality evolution of palaeocene deep-water, marine sandstones, the shetland-faroes basin, British continental shelf. Mar. Petrol. Geol. 25 (6), 514–543. https://doi.org/10.1016/j.marpetgeo.2007.07.012.
Mietto, P., Jin, X., Manfrin, S., et al., 2021. Onset of sedimentation near the carnian/norian boundary in the Northwestern Sichuan Basin: New evidence from ammonoid biostratigraphy and zircon U-Pb geochronology. Palaeogeogr. Palaeoclimatol. Palaeoecol. 567, 110246. https://doi.org/10.1016/j.palaeo.2021.110246.
Morad, S., Al-Ramadan, K., Ketzer, J.M., et al., 2010. The impact of diagenesis on the heterogeneity of sandstone reservoirs: A review of the role of depositional facies and sequence stratigraphy. AAPG Bull. 94 (8), 1267–1309. https://doi.org/10.1306/04211009178.
Nance, W.B., Taylor, S.R., 1976. Rare earth element patterns and crustal evolution—I. Australian post-Archean sedimentary rocks. Geochim. Cosmochim. Acta 40 (12), 1539–1551. https://doi.org/10.1016/0016-7037(76)90093-4.
Oluwadebi, A.G., Taylor, K.G., Dowey, P.J., 2018. Diagenetic controls on the reservoir quality of the tight gas collyhurst sandstone formation, Lower Permian, east Irish Sea Basin, United Kingdom. Sediment. Geol. 371, 55–74. https://doi.org/10.1016/j.sedgeo.2018.04.006.
Pang, H., Huo, X., Pang, X., et al., 2023. Quantitative characterization of critical reservoir physical properties of tight oil charging in the third member of the Shahejie Formation in the gaobei slope of Nanpu sag, Bohai Bay Basin. Geoenergy Sci. Eng. 230, 212212. https://doi.org/10.1016/j.geoen.2023.212212.
Peltonen, C., Marcussen, Ø., Bjørlykke, K., et al., 2009. Clay mineral diagenesis and quartz cementation in mudstones: The effects of smectite to illite reaction on rock properties. Mar. Petrol. Geol. 26 (6), 887–898. https://doi.org/10.1016/j.marpetgeo.2008.01.021.
Phan, T.T., Hakala, J.A., Lopano, C.L., et al., 2019. Rare earth elements and radiogenic strontium isotopes in carbonate minerals reveal diagenetic influence in shales and limestones in the appalachian basin. Chem. Geol. 509, 194–212. https://doi.org/10.1016/j.chemgeo.2019.01.018.
Qian, W., Yin, T., Zhang, C., et al., 2020. Diagenesis and diagenetic stages prediction of Ed2 reservoir in the west of Bozhong sag. Petroleum 6 (1), 23–30. https://doi.org/10.1016/j.petlm.2019.04.003.
Qin, S., Li, F., Li, W., et al., 2018. Formation mechanism of tight coal-derived-gas reservoirs with medium-low abundance in Xujiahe Formation, central Sichuan Basin. China. Mar. Petrol. Geol. 89, 144–154. https://doi.org/10.1016/j.marpetgeo.2017.06.032.
Rahman, M.J.J., McCann, T., 2012. Diagenetic history of the surma group sandstones (Miocene) in the surma basin, Bangladesh. J. Asian Earth Sci. 45, 65–78. https://doi.org/10.1016/j.jseaes.2011.09.019.
Rezaee, M.R., Tingate, P.R., 1997. Origin of quartz cement in the tirrawarra sandstone, Southern cooper Basin, South Australia. J. Sediment. Res. 67 (1), 168–177. https://doi.org/10.1306/D4268522-2B26-11D7-8648000102C1865D.
Schmid, S., Worden, R.H., Fisher, Q.J., 2004. Diagenesis and reservoir quality of the sherwood sandstone (Triassic), corrib field, Slyne Basin, west of Ireland. Mar. Petrol. Geol. 21 (3), 299–315. https://doi.org/10.1016/j.marpetgeo.2003.11.015.
Schmid, S., Worden, R.H., Fisher, Q.J., 2006. Carbon isotope stratigraphy using carbonate cements in the Triassic sherwood sandstone group: Corrib field, West of Ireland. Chem. Geol. 225 (1–2), 137–155. https://doi.org/10.1016/j.chemgeo.2005.09.006.
Shen, Z., Ruan, Z., Yu, B., et al., 2022. Diagenetic fluid and Its impact on sandstone reservoirs in the southern Boxing sag, Dongying depression, Bohai Bay Basin, China. Geofluids 2022 (1), 4981422. https://doi.org/10.1155/2022/4981422.
Shi, H., Luo, X., Lei, G., et al., 2017. Diagenesis and fluid flow variability of structural heterogeneity units in tight sandstone carrier beds of dibei, eastern kuqa depression. Geofluids 2017 (1), 6593913. https://doi.org/10.1155/2017/6593913.
Song, Y., Zhao, M., Fang, S., et al., 2012. Dominant factors of hydrocarbon distribution in the foreland basins, central and western China. Petrol. Explor. Dev. 39 (3), 285–294. https://doi.org/10.1016/S1876-3804(12)60044-5.
Stroker, T.M., Harris, N.B., Crawford Elliott, W., et al., 2013. Diagenesis of a tight gas sand reservoir: Upper Cretaceous mesaverde group, Piceance Basin, Colorado. Mar. Petrol. Geol. 40, 48–68. https://doi.org/10.1016/j.marpetgeo.2012.08.003.
Sun, F., Hu, W., Wu, H., et al., 2021. Two-stage mineral dissolution and precipitation related to organic matter degradation: insights from in situ C–O isotopes of zoned carbonate cements. Mar. Petrol. Geol. 124, 104812. https://doi.org/10.1016/j.marpetgeo.2020.104812.
Sun, T., Luo, X., Mi, W., et al., 2023. Characterization of ultra-deeply buried middle Triassic leikoupo marine carbonate petroleum system (!) in the Western Sichuan depression. China. Mar. Petrol. Geol. 150, 106099. https://doi.org/10.1016/j.marpetgeo.2023.106099.
Swart, P.K., 2015. The geochemistry of carbonate diagenesis: The past, present and future. Sedimentology 62 (5), 1233–1304. https://doi.org/10.1111/sed.12205.
Sylvestre, G., Laure, N.T.E., Djibril, K.N.G., et al., 2017. A mixed seawater and hydrothermal origin of superior-type banded iron formation (BIF)-hosted kouambo iron deposit, palaeoproterozoic nyong series, Southwestern Cameroon: constraints from petrography and geochemistry. Ore Geol. Rev. 80, 860–875. https://doi.org/10.1016/j.oregeorev.2016.08.021.
Tan, D., Luo, L., Song, L., et al., 2023. Differential precipitation mechanism of cement and its impact on reservoir quality in tight sandstone: A case study from the Jurassic Shaximiao Formation in the central Sichuan Basin, SW China. Geoenergy Sci. Eng. 221, 111263. https://doi.org/10.1016/j.petrol.2022.111263.
Taylor, K.G., Gawthorpe, R.L., Curtis, C.D., et al., 2000. Carbonate cementation in a sequence-stratigraphic framework: Upper Cretaceous sandstones, book cliffs, Utah-Colorado. J. Sediment. Res. 70 (2), 360–372. https://doi.org/10.1306/2DC40916-0E47-11D7-8643000102C1865D.
Taylor, T.R., Giles, M.R., Hathon, L., et al., 2010. Sandstone diagenesis and reservoir quality prediction: Models, myths, and reality. AAPG Bull. 94 (8), 1093–1132. https://doi.org/10.1306/04211009123.
Wang, Y., Zhang, K., Gan, Q., et al., 2015. Fracture development characteristics in the Upper Triassic Xujiahe Formation, western Sichuan Depression (China). J. Pet. Sci. Eng. 135, 542–551. https://doi.org/10.1016/j.petrol.2015.10.016.
Wang, J., Cao, Y., Liu, K., et al., 2016. Pore fluid evolution, distribution and water-rock interactions of carbonate cements in red-bed sandstone reservoirs in the dongying depression. China. Mar. Petrol. Geol. 72, 279–294. https://doi.org/10.1016/j.marpetgeo.2016.02.018.
Wang, J., Cao, Y., Liu, K., et al., 2019. Mass transfer between mudstone-sandstone interbeds during diagenesis as revealed from the type and distribution of carbonate cements in the Eocene beach-bar sandstones, Bohai Bay Basin. Mar. Petrol. Geol. 110, 21–34. https://doi.org/10.1016/j.marpetgeo.2019.07.005.
Wang, Q., Chen, D., Gao, X., et al., 2020. Microscopic pore structures of tight sandstone reservoirs and their diagenetic controls: A case study of the Upper Triassic Xujiahe Formation of the Western Sichuan depression. China. Mar. Petrol. Geol. 113, 104119. https://doi.org/10.1016/j.marpetgeo.2019.104119.
Wang, Z., Hao, C., Jin, H., et al., 2023. Geochemical characteristics and hydrocarbon generation potential of main source rocks in the Upper Triassic Xujiahe Formation, Sichuan Basin, China. Front. Earth Sci. 11, 1233959. https://doi.org/10.3389/feart.2023.1233959.
Weislogel, A.L., Graham, S.A., Chang, E.Z., et al., 2006. Detrital zircon provenance of the Late Triassic songpan-ganzi complex: Sedimentary record of collision of the north and south China blocks. Geology 34 (2), 97–100. https://doi.org/10.1130/G21929.1.
Worden, R., Morad, S., 2000. Quartz cementation in oil field sandstones: A review of the key controversies. Spec. Publ. Int. Assoc. Sed. 29, 1–20. https://doi.org/10.1002/9781444304237.ch1.
Wu, X., Chen, Y., Wang, Y., et al., 2021. Geochemical characteristics of natural gas in tight sandstone of the Chengdu large gas field, Western Sichuan depression, Sichuan Basin, China. J. Nat. Gas Geosci. 6 (5), 279–287. https://doi.org/10.1016/j.jnggs.2021.09.003.
Xi, K., Cao, Y., Jahren, J., et al., 2015. Diagenesis and reservoir quality of the Lower Cretaceous quantou formation tight sandstones in the southern Songliao Basin, China. Sediment. Geol. 330, 90–107. https://doi.org/10.1016/j.sedgeo.2015.10.007.
Xi, K., Cao, Y., Liu, K., et al., 2019. Diagenesis of tight sandstone reservoirs in the Upper Triassic Yanchang Formation, Southwestern Ordos Basin. China. Mar. Petrol. Geol. 99, 548–562. https://doi.org/10.1016/j.marpetgeo.2018.10.031.
Xi, K., Cao, Y., Haile, B.G., et al., 2021. Diagenetic variations with respect to sediment composition and paleo-fluids evolution in conglomerate reservoirs: A case study of the Triassic baikouquan Formation in Mahu Sag, Junggar Basin, Northwestern China. J. Pet. Sci. Eng. 197, 107943. https://doi.org/10.1016/j.petrol.2020.107943.
Xiao, D., Cao, J., Luo, B., et al., 2020. On the dolomite reservoirs formed by dissolution: Differential eogenetic versus hydrothermal in the lower Permian Sichuan basin, Southwestern China. AAPG Bull. 104 (7), 1405–1438. https://doi.org/10.1306/02262018242.
Xiong, D., Azmy, K., Blamey, N.J.F., 2016. Diagenesis and origin of calcite cement in the Flemish pass basin sandstone reservoir (Upper Jurassic): Implications for porosity development. Mar. Petrol. Geol. 70, 93–118. https://doi.org/10.1016/j.marpetgeo.2015.11.013.
Xu, Z., Liu, L., Jiang, S., et al., 2019. Migration model of hydrocarbons in the slope of the superimposed foreland basin: A study from the south Junggar, NW China. J. Pet. Sci. Eng. 182, 106337. https://doi.org/10.1016/j.petrol.2019.106337.
Xu, X., Zhang, L., Zeng, L., et al., 2023. Effects of overpressure on deep sandstone reservoir quality: a case study of the medium and Lower Jurassic Formation in the Shawan Sag, central Junggar Basin, Western China. Geoenergy Sci. Eng. 230, 212203. https://doi.org/10.1016/j.geoen.2023.212203.
Yang, P., Zhang, L., Liu, K., et al., 2021. Diagenetic history and reservoir evolution of tight sandstones in the second member of the Upper Triassic Xujiahe Formation, western Sichuan Basin, China. J. Pet. Sci. Eng. 201, 108451. https://doi.org/10.1016/j.petrol.2021.108451.
Yin, F., Liu, R., Qin, H., 2013. About origin of tight sandstone gas: To discuss with academician Dai Jinxing. Petrol. Explor. Dev. 40 (1), 134–138. https://doi.org/10.1016/S1876-3804(13)60016-6.
Yu, Y., Lin, L., Zhai, C., et al., 2019. Impacts of lithologic characteristics and diagenesis on reservoir quality of the 4th member of the Upper Triassic Xujiahe Formation tight gas sandstones in the Western Sichuan Basin, Southwest China. Mar. Petrol. Geol. 107, 1–19. https://doi.org/10.1016/j.marpetgeo.2019.04.040.
Yu, Y., Lin, L., Li, Z., et al., 2022. Source of quartz cement in tight gas sandstone: evidence from the Upper Triassic Xujiahe Formation in the Western Sichuan Basin, SW China. J. Pet. Sci. Eng. 212, 110299. https://doi.org/10.1016/j.petrol.2022.110299.
Yuan, G., Cao, Y., Schulz, H.-M., et al., 2019. A review of feldspar alteration and its geological significance in sedimentary basins: Fom shallow aquifers to deep

hydrocarbon reservoirs. Earth Sci. Rev. 191, 114–140. https://doi.org/10.1016/j.earscirev.2019.02.004.
Zelilidis, A., Maravelis, A.G., 2015. Introduction to the thematic issue: adriatic and Ionian seas: Proven petroleum systems and future prospects. J. Pet. Geol. 38 (3), 247–253. https://doi.org/10.1111/jpg.12609.
Zhang, Y., Pe-Piper, G., Piper, D.J.W., 2015. How sandstone porosity and permeability vary with diagenetic minerals in the Scotian Basin, offshore eastern Canada: Implications for reservoir quality. Mar. Petrol. Geol. 63, 28–45. https://doi.org/10.1016/j.marpetgeo.2015.02.007.
Zhang, D., 2022. Development prospect of natural gas industry in the Sichuan Basin in the next decade. Nat. Gas. Ind. B. 9 (2), 119–131. https://doi.org/10.1016/j.ngib.2021.08.025.
Zhao, Y., Li, S., Li, D., et al., 2019. Rare earth element geochemistry of carbonate and its paleoenvironmental implications. Geotect. Metallog. 43 (1), 141–167. https://doi.org/10.16539/j.ddgzyckx.2019.01.011.
Zhao, S., Fu, Q., Fu, J., et al., 2022. Effect of authigenic clay minerals and carbonate cements on quality of tight sandstone reservoirs: insight from Triassic tight sandstones in the Huaqing area, Ordos Basin, Northern China. J. Asian Earth Sci. 229, 105099. https://doi.org/10.1016/j.jseaes.2022.105099.
Zheng, D., Pang, X., Ma, X., et al., 2019. Hydrocarbon generation and expulsion characteristics of the source rocks in the third member of the Upper Triassic Xujiahe Formation and its effect on conventional and unconventional hydrocarbon resource potential in the Sichuan Basin. Mar. Petrol. Geol. 109, 175–192. https://doi.org/10.1016/j.marpetgeo.2019.06.014.
Zheng, T., Ma, X., Pang, X., et al., 2020. Hydrocarbon generation and expulsion features of the Upper Triassic Xujiahe Formation source rocks and their controlling effects on hydrocarbon accumulation in the Sichuan basin, central China. Geol. J. 55 (7), 4977–4996. https://doi.org/10.1002/gj.3653.
Zhong, Y., Huang, K., Ye, L., et al., 2020. Diagenesis of tight sandstone reservoirs of Xujiahe fFormation (Upper Triassic), the Xinchang gas field, western Sichuan Basin, China. Geol. J. 55 (6), 4604–4624. https://doi.org/10.1002/gj.3689.
Zou, C., Tao, S., Zhu, R., et al., 2009. Formation and distribution of “continuous” gas reservoirs nd their giant gas province: a case from the upper Riassic Xujiahe Formation giant gas province, Sichuan Basin. Petrol. Explor. Dev. 36 (3), 307–319. https://doi.org/10.1016/S1876-3804(09)60128-2.
Zou, C., Zhu, R., Liu, K., et al., 2012. Tight gas sandstone reservoirs in China: Characteristics and recognition criteria. J. Pet. Sci. Eng. 88–89, 82–91. https://doi.org/10.1016/j.petrol.2012.02.001.